

41th European Rotorcraft Forum  
September 1-4,2014, Munich, Germany

## Effect of Active Gurney Flaps on Overall Helicopter Flight Envelope

Vasileios Pastrikakis, René Steijl and George N. Barakos

CFD Laboratory, School of Engineering  
University of Liverpool, L69 3GH, U.K.

<http://www.liv.ac.uk/flightscience/PROJECTS/CFD/ROTORCRAFT/RBD/index.htm>

Email: [G.Barakos@liverpool.ac.uk](mailto:G.Barakos@liverpool.ac.uk)

### Abstract

This paper presents a study of the W3-Sokol main rotor equipped with Gurney flaps. The effect of the active Gurney is tested at low and high forward flight speeds to draw conclusions about the potential enhancement of the rotorcraft performance for the whole flight envelope. The effect of the flap on the trimming and handling of a full helicopter is also investigated. Fluid and structure dynamics were coupled in all cases, and the rotor was trimmed at different thrust coefficients. The Gurney proved to be efficient at medium to high advance ratios, where the power requirements of the rotor were decreased by up to 3.3%. However, the 1/rev actuation of the flap might be an issue for the trimming and handling of the helicopter. The current study builds on the idea that any active mechanism operating on a rotor could alter the dynamics and the handling of the helicopter. A closed loop actuation of the Gurney flap was put forward based on a pressure divergence criterion, and it led to further enhancement of the aerodynamic performance. Next, a generic light utility helicopter was built using 2D aerodynamics of the main aerofoil section of the W3 Sokol blade along with a robust controller, and the response of the rotorcraft to control inputs was tested. This analysis proved that the 1/Rev actuation of the Gurney did not alter the handling qualities of the helicopter, and as a result it can be implemented as a flow control mechanism for aerodynamic enhancement and retreating blade stall alleviation.

### NOTATION

#### LATIN

|                    |   |   |
|--------------------|---|---|
| $a$                | = | Angle of incidence (degrees)                                      |
| $c$                | = | Chord in untapered part of the blade (m)                          |
| $k$                | = | Turbulent kinetic energy  |
| $l$                | = | Characteristic scale of the flow (main chord at this study) (m)   |
| $v$                | = | Mean velocity of the blade section relative to the fluid (m/s)    |
| $a_{\text{sound}}$ | = | Speed of sound (m/s)  |
| $c_p$              | = | Pressure coefficient  |
| $C_T$              | = | Thrust coefficient, $C_T = T / (0.5\rho\pi R^2 V_{\text{tip}}^2)$ |
| $C_Q$              | = | Torque coefficient, $C_Q = Q / (0.5\rho\pi R^3 V_{\text{tip}}^2)$ |
| $E$                | = | Total internal energy per unit mass                               |
| $M$                | = | Mach number ( $v/a_{\text{sound}}$ )                              |
| $N_b$              | = | Number of blades  |
| $P_i$              | = | Ideal induced rotor power   |
| $P$                | = | Actual rotor power  |
| $R$                | = | Aspect ratio of the blade   |
| $V(t)$             | = | Time dependent control volume                                     |
| $Re$               | = | Reynolds Number ( $vl/\nu$ )                                      |
| $FM$               | = | Figure of merit, $FM = P_i/P$                                     |
| $BVI$              | = | Blade Vortex Interaction  |
| $MRB$              | = | Main Rotor Blade  |
| $CFD$              | = | Computational Fluid Dynamics                                      |
| $CVT$              | = | Constant Volume Tetrahedral                                       |
| $PIV$              | = | Particle Image Velocimetry  |
| $SAM$              | = | Spring Analogy Method   |
| $TFI$              | = | Transfinite Interpolation   |
| $\vec{R}_{i,j,k}$  | = | Flux residuals at cell (i, j, k)                                  |
| $\vec{w}$          | = | Vector of conserved variables                                     |

|              |   |  |
|--------------|---|--|
| $\vec{F}a_i$ | = | Inviscid fluxes                          |
| $\vec{F}a_v$ | = | Viscous fluxes                           |
| $\vec{n}a_i$ | = | Normal vector of the i-th face of a cell |
| $\vec{S}$    | = | Source term                              |

#### Subscripts

|          |   |                     |
|----------|---|---------------------|
| $\infty$ | = | Free-stream Value   |
| $tip$    | = | Tip value           |
| $tpp$    | = | Tip path plane      |
| $nfp$    | = | No feathering plane |

#### GREEK

|                        |   |  |
|------------------------|---|--|
| $\alpha$               | = | Lift slope (rad)                                       |
| $\beta$ or $\beta_0$   | = | Flapping angle (degrees)                               |
| $\gamma$               | = | Rotor blade Lock number, $(\phi\alpha cR^4/I_b)$       |
| $\theta$ or $\theta_0$ | = | Collective angle at 75%R (degrees)                     |
| $\lambda$              | = | Inflow factor  |
| $\nu$                  | = | Kinematic viscosity, $(\mu_v/\rho, m^2/s)$             |
| $\mu$                  | = | Advance ratio  |
| $\mu_v$                | = | Dynamic viscosity (kg/ms)                              |
| $\rho$                 | = | Density (kg/m <sup>3</sup> )                           |
| $\sigma$               | = | Rotor solidity, $(N_b cR/\pi R^2)$                     |
| $\omega$               | = | Specific dissipation (m <sup>2</sup> /s <sup>3</sup> ) |
| $\vec{\omega}$         | = | Rotor rotational speed                                 |

# 1 INTRODUCTION

Losses due to flow separation are detrimental to rotor performance and normally occur at the retreating side of the rotor disk where the blade is required to operate at higher angles of attack to balance the rotor disk loads. Retreating blade stall results in highly unsteady flow, and introduces vibration. Thus, controlling the flow separation is essential. Gurney flaps are capable of providing extra lift at pitch angles below stall. The purpose of the study is to investigate the possibility of implementing an active Gurney flap on a rotor blade for controlling the retreating blade stall without altering the dynamics of the helicopter.

## 1.1 Gurney flaps

The use of Gurney flaps for lift enhancement is well established in the aerospace community and several research works e.g. by Wang et al. [1] document the advantages and disadvantages of these devices. The Gurney flap was introduced by Dan Gurney and its aerodynamics was first studied by Liebeck [2]. This has been followed by numerous experimental studies by Jeffrey and Zghang [3], Trooling et al. [4], and Lee and Su [5]. Tang and Dowell [6] compared the loading of a NACA0012 wing section with both static and oscillating trailing-edge Gurney flaps using an incompressible Navier-Stokes code against experiments conducted in a wind tunnel by them. Due to the scarcity of experimental data with dynamically deployed Gurney flaps Chow and Van Dam [7], Baker et al. [8], and Kinzel et al. [9] have utilised this set of data in their computational studies.

The Gurney flap is a short flat plate placed at the trailing edge, perpendicular to the chord-line on the pressure side of the aerofoil, and works by providing a stagnation area near the trailing edge resulting in an increase of lift. It increases the zero lift angle and keeps the lift slope constant so there is a decrease in the stall angle. The pitching moment coefficient is also increased (i.e. more nose down) as presented by Gai and Palfrey [10], and unless the Gurney is sized carefully, substantial drag penalties may also occur. Based on the review of flow control mechanisms by Yeo [11] Gurney flaps are generally less than 3% of the wing chord. Previous studies by Jeffrey et al. [12], and Maughmer and Bramesfeld [13] have concluded that the optimal height for a Gurney flap should be close to the boundary layer thickness on the pressure side of the aerofoil. If the Gurney flap height is smaller than the boundary layer thickness, then its influence is significantly decreased, while increasing the size of the flap leads to a drag penalty.

Most of the studies found in the literature are dealing with commonly used aerofoils in rotorcraft applications and try to derive conclusions concerning the potential effect of the Gurney flap on rotor blades according to two-dimensional calculations. Min et al. [14] studied the effects of Gurney flaps on the blade root loads and hub vibratory loads. In their study, a Gurney flap was deployed over the entire span of the BO-105 rotor in forward flight with three different deployment schedules. A carefully chosen azimuthal deployment schedule of the Gurney flap was found to reduce the peak-to-peak variations in hub loads. The 4-per-revolution normal force at the hub was compared with the loads for a higher harmonic controlled rotor and the baseline rotor. The simulations showed that the Gurney flap deployment reduced the 4-per-rev normal force vibration by 80%. For the same rotor in descending flight, a Gurney set at 30 degrees angle relative to the mean chord resulted in a 40% decrease of the vertical descend rate. However, the Gurney flap resulted in local nose-down pitching moment, which indicates that additional fluid-structure coupling analysis for aeroelastic deformation is required.

Active Gurney flaps were also studied by Padthe et al. [15] to determine their effectiveness in reducing noise and vibration in rotorcraft, as well as improving rotor performance. Active control studies employing microflaps were conducted on a hingeless rotor configuration resembling the MBB BO-105, and various spanwise configurations of the flaps, including a single, a dual, and a segmented five-flap configuration were evaluated. Results indicate that the Gurney flap is capable of substantial reductions in blade vortex interaction (BVI) noise ranging from 3-6 dB. Vibration reduction ranging from 70-90% was also demonstrated. Vibration and noise reduction was also examined at the same time, and was found that reduction in one was linked to an increase on the other. Finally, the Gurney flap appeared to be more effective in reducing the BVI noise at both advancing and retreating sides while the plain flap was more effective in reducing the vibrations.

The effectiveness of a single active Gurney flap in reducing vibration of a UH-60A Blackhawk helicopter in high-speed flight ( $\mu = 0.35$ ) was studied by Bae and Gandhi [16] based on a 2D Navier Stokes CFD code. An elastic blade was considered and the Gurney flap was extending from 70%R to 80%R and was deployed to an amplitude of 0.5% of the chord. The Gurney flap actuation was most influential in reducing the vertical vibratory hub force. The most effective actuation input was 4/rev and it led to 80% reduction.

Comparing the above studies [14–16] to the ones conducted by Milgram et al. [17], and Viswamurthy and Ganguli [18] it seems that a Gurney flap can have a similar effect on the vibratory loads of the rotor hub like a conventional trailing edge flap. Such a flap is used on a soft hingeless rotor [18] leading to a 72% reduction of the vibratory loads. However, the advantage of using a Gurney flap compared to a trailing edge flap may be on the amount of energy required for the actuation and the ease of the implementation of the Gurney flap.

A further computational study [19] tried to assess active control mechanisms for rotor performance enhancement. A four-bladed rotor was considered at medium (80kt) and high (150kt) speed forward flight cases and the Gurney flap was assumed to be either completely deployed or retracted. A significant increase in thrust for a given power was found when the Gurney was extended from 60%R up to 100%R, and activated at the retreating side, which agrees with the outcome of the study by Cheng and Celi [20] who defined the optimum 2-per-revolution inputs in order to improve the rotor performance by either increasing the thrust of the rotor or decreasing the torque requirement. However, the positive effect of the Gurney was observed at medium

flight speeds while at high speed the performance improvement diminished.

Gagliardi and Barakos [21] studied a low twist hovering rotor and the effects of trailing-edge flaps on its performance. A flap located inboard resulted in hover performance similar to a blade of 6 deg more twist. At the same time, a reduction of the trim angles was observed. A flap located outboard did not improve the performance of the rotor although by carefully optimising its configuration similar trim benefits as for the inboard flap were achieved.

The majority of the previous studies are computational and there is a need for experimental investigations of Gurney flaps on rotors. There is, however, an experimental and computational study of the aeromechanics of a Sikorsky demonstration rotor [22] that examined the effect of an active flap. The report points out that the Gurney flap may have similar effect to a conventional flap. However, because of its small size the Gurney has the potential for high bandwidth active control with low actuation power requirements and minimal impact to the blade structure when compared to conventional control surfaces.

To conclude, few complete studies concerning Gurney flap implementation on helicopter rotors were found in the literature. All of them investigated the effect of Gurneys on BVI and/or vibration reduction in forward flight, while Pstrikakis et al. [23] demonstrated the potential effect of Gurney flaps on a hovering rotor. Although there is strong indication from 2D calculations of potential performance enhancement the question still remains whether there is a practical forward flight benefit to be achieved. In this work, an active Gurney flap is studied on the main rotor blade of the W3 Sokol helicopter. The enhancement of the performance is investigated by coupling fluid and structure calculations taking into account the structural properties of the main rotor blade (MRB). The method used for the CFD-CSD coupling was presented in detail in the previous studies of aeroelastic rotors [24–26]. To the authors’ knowledge this is the first effort to investigate the potential effect of a Gurney flap on the overall envelope of a helicopter along with the flap’s effect on the dynamics of a full helicopter model.

## 2 NUMERICAL METHODS

### 2.1 HMB2 flow solver

The HMB2 CFD solver [27–29] was employed for this work. HMB2 solves the Navier-Stokes equations in integral form using the arbitrary Lagrangian Eulerian formulation for time-dependent domains with moving boundaries:

$$\frac{d}{dt} \int_{V(t)} \vec{w} dV + \int_{\partial V(t)} (\vec{F}_i(\vec{w}) - \vec{F}_v(\vec{w})) \vec{n} dS = \vec{S}. \quad (1)$$

The above equations form a system of conservation laws for any time-dependent control volume  $V(t)$  with boundary  $\partial V(t)$  and outward unit normal  $\vec{n}$ . The vector of conserved variables is denoted by  $\vec{w} = [\rho, \rho u, \rho v, \rho w, \rho E]^T$ , where  $\rho$  is the density,  $u, v, w$  are the Cartesian velocity components and  $E$  is the total internal energy per unit mass.  $\vec{F}_i$  and  $\vec{F}_v$  are the inviscid and viscous fluxes, respectively. For hovering rotors, the grid is fixed, and a source term,  $\vec{S} = [0, -\rho \vec{\omega} \times \vec{u}_h, 0]^T$ , is added to compensate for the inertial effects of the rotation.  $\vec{u}_h$  is the local velocity field in the rotor-fixed frame of reference.

The non-inertial frame of reference used here has two benefits over a rotating frame of reference: firstly, the energy equation is unchanged by the rotation vector  $\vec{\omega}$  and, secondly, a vanishing ‘undisturbed’ velocity field occurs in contrast to the position-dependent ‘undisturbed’ velocity field in the rotating frame of reference, which is given by  $-\vec{\omega} \times \vec{r}$ .

Equations (1) are discretized using a cell-centred finite volume approach on structured multiblock grids. The spatial discretisation leads to a set of equations in time,

$$\frac{\partial}{\partial t} (\vec{w}_{i,j,k} V_{i,j,k}) = -\vec{R}_{i,j,k}(\vec{w}_{i,j,k}), \quad (2)$$

where  $\vec{w}$  and  $\vec{R}$  are the vectors of cell variables and residuals, respectively. Here,  $i,j,k$  are the cell indices in each of the grid blocks, and  $V_{i,j,k}$  is the cell volume. The convective terms are discretized using Osher’s upwind scheme [30], MUSCL variable interpolation is used to provide high order accuracy and the Van Albada limiter [31] is employed to prevent spurious oscillations near steep gradients. Boundary conditions are set using ghost cells on the exterior of the computational domain. For viscous flow simulations, ghost values are extrapolated at solid boundaries ensuring that the velocity takes on the solid wall velocity. Implicit time integration is employed, and the resulting linear system of equations is solved using a pre-conditioned Generalised Conjugate Gradient method. For unsteady simulations, an implicit dual-time stepping method is used, based on the pseudo-time integration approach by Jameson [32]. The HMB2 method has been validated for a range of rotorcraft applications and has demonstrated good accuracy and efficiency for very demanding flows. Examples of work with HMB2 can be found in references [27, 28, 33]. Several rotor trimming methods are available in HMB2 along with a blade-actuation algorithm that allows for the near-blade grid quality to be maintained on deforming meshes [27].

The HMB2 solver has a library of turbulence closures including several one- and two- equation turbulence models and even non-Boussinesq versions of the  $k - \omega$  model that is used for this work. Turbulence simulation is also possible using either the Large-Eddy or the Detached-Eddy approach. The solver was designed with parallel execution in mind and the MPI library along with a load-balancing algorithm are used to this end. For multi-block grid generation, the ICEM-CFD Hexa commercial meshing tool is used and CFD rotor grids with 10-30 million points and thousands of blocks are commonly used.

For forward flying rotors, the HMB2 solves the compressible-flow Reynolds-Averaged Navier-Stokes equations in an inertial frame of reference. The employed finite-volume discretisation accounts for moving and deforming meshes in time-accurate

simulations. Consequently, a rotor in forward flight is modelled in a ‘helicopter-fixed frame of reference’, where the forward flight velocity is introduced through the definition of the ‘free-stream’ conditions. For isolated rotors, as well as, rotor/fuselage or rotor/wind-tunnel cases, the rotor and rotor blade motions are then accounted for using mesh velocities. For rotor/fuselage or rotor/wind-tunnel cases, the relative motion of the rotor and the fixed fuselage or tunnel is accounted for the sliding-plane approach [28].

## 2.2 Modelling Gurney flaps

For the purposes of this study the effect of the Gurney flap on W3-Sokol MRB is modelled by flagging any block face within the computational mesh occupied by the flap with a solid, no slip boundary condition. This method is implemented in the HMB2 solver and is proved to be simple and effective [34, 35]. To be able to obtain the loads on the Gurney flap alone and to be able to find its moment about a different point - for example the Gurney’s hinge - HMB2 requires some additional information. Firstly, a special boundary condition tag must be used for the Gurney flap to be identified. Secondly, additional input files must be used to inform HMB2 that computations are to be performed with a Gurney flap. The advantage of this method is that no additional effort is needed in terms of mesh generation. On the other hand, the Gurney is assumed to have no thickness. In case of an actuated Gurney flap a method with overset grids would be required. Otherwise, the deformation of the mesh near the flap would alter the quality of the mesh a lot. Modelling the effect of the flap as stated above allows the mesh quality to remain the same as the mesh do not deforms along with the actuation of the flap.

## 2.3 Trimming Method

The trimmer used for this study is based on the blade element theory and is described by Steijl et al. [36]. The trimming method consists of an initial trim-state computation and a number of subsequent re-trimming steps. The initial trim state can be obtained either off-line or within the CFD solver. During re-trimming, the collective pitch is updated via a Newton-Raphson process, where the simple aerodynamic model is only used to compute the derivatives of the loads. As a result, upon convergence, the trim state is independent of the approximate aerodynamics. For simulations of forward-flying rotors, re-trimming is carried out after completion of 1 rotor revolution using revolution-averaged integrated loads from CFD solution. The trimming method needs a target thrust coefficient  $c_T$  as input. For this study the thrust estimate is given based on the flight tests. In addition, models for the fuselage and its drag are necessary in order to compute the total drag, as a function of the advance ratio of the helicopter. From the rotor thrust and total drag, the orientation of the tip-path plane can be obtained, i.e. the forward tilt. For a rotor at straight level conditions the orientation of the tip-path plane can be obtained from  $\sin\theta_{\text{tip}} = -D/W$ , where  $D$  and  $W$  represent the total drag of the helicopter and its weight.

Assuming a fixed rotor shaft angle  $\theta_{\text{shaft}}$  and known first harmonic flap coefficients  $\beta_{1s}$  and  $\beta_{1c}$ , the thrust and moment coefficients can be expressed as a function of collective and cyclic pitch angles:

$$\begin{aligned} C_T &= C_T(\theta_0, \theta_{1c}, \theta_{1s}) \\ C_{M,x} &= C_{M,x}(\theta_0, \theta_{1c}, \theta_{1s}) \\ C_{M,y} &= C_{M,y}(\theta_0, \theta_{1c}, \theta_{1s}) \end{aligned}$$

where  $C_{M,x}$  and  $C_{M,y}$  are the non-dimensional moments about the  $x$ -axis (rotor disk rolling moment) and  $y$ -axis (rotor disk pitching moment), respectively.

$$\begin{pmatrix} \Delta\theta_0 \\ \Delta\theta_{1s} \\ \Delta\theta_{1c} \end{pmatrix} = \begin{pmatrix} \frac{\partial C_T}{\partial \theta_0} & \frac{\partial C_T}{\partial \theta_{1s}} & \frac{\partial C_T}{\partial \theta_{1c}} \\ \frac{\partial C_{M,x}}{\partial \theta_0} & \frac{\partial C_{M,x}}{\partial \theta_{1s}} & \frac{\partial C_{M,x}}{\partial \theta_{1c}} \\ \frac{\partial C_{M,y}}{\partial \theta_0} & \frac{\partial C_{M,y}}{\partial \theta_{1s}} & \frac{\partial C_{M,y}}{\partial \theta_{1c}} \end{pmatrix}^{-1} \begin{pmatrix} C_{T,target} - C_T \\ C_{M_x,target} - C_{M_x} \\ C_{M_y,target} - C_{M_y} \end{pmatrix} \quad (3)$$

The elements of the sensitivity matrix in Equation (3) are the derivatives of  $C_T$ ,  $C_{M,x}$  and  $C_{M,y}$  according to blade-element theory. Assuming a constant inflow factor  $\lambda$  and fixed flapping harmonics, the sensitivity matrix reads:

$$\begin{pmatrix} \frac{\partial C_T}{\partial \theta_0} & \frac{\partial C_T}{\partial \theta_{1s}} & \frac{\partial C_T}{\partial \theta_{1c}} \\ \frac{\partial C_{M,x}}{\partial \theta_0} & \frac{\partial C_{M,x}}{\partial \theta_{1s}} & \frac{\partial C_{M,x}}{\partial \theta_{1c}} \\ \frac{\partial C_{M,y}}{\partial \theta_0} & \frac{\partial C_{M,y}}{\partial \theta_{1s}} & \frac{\partial C_{M,y}}{\partial \theta_{1c}} \end{pmatrix} = \frac{\sigma a}{4} \begin{pmatrix} (\frac{2}{3} + \mu^2) & -\mu & 0 \\ \frac{2}{3}\mu & -\frac{1}{4}(1 + \frac{3}{2}\mu^2) & 0 \\ 0 & 0 & \frac{1}{4}(1 + \frac{1}{2}\mu^2) \end{pmatrix} \quad (4)$$

Solving equation 3 gives:

$$\begin{aligned}
\Delta\theta_0 &= \left[ \frac{\partial C_T}{\partial \theta_0} \frac{\partial C_{M,x}}{\partial \theta_{1s}} - \frac{\partial C_T}{\partial \theta_{1s}} \frac{\partial C_{M,x}}{\partial \theta_0} \right]^{-1} \left( \frac{\partial C_{M,x}}{\partial \theta_{1s}} (C_{T,target} - C_T) + \frac{\partial C_T}{\partial \theta_{1s}} C_{M,x} \right) \\
\Delta\theta_{1s} &= \left[ \frac{\partial C_T}{\partial \theta_0} \frac{\partial C_{M,x}}{\partial \theta_{1s}} - \frac{\partial C_T}{\partial \theta_{1s}} \frac{\partial C_{M,x}}{\partial \theta_0} \right]^{-1} \left( -\frac{\partial C_{M,x}}{\partial \theta_0} (C_{T,target} - C_T) - \frac{\partial C_T}{\partial \theta_0} C_{M,x} \right) \\
\Delta\theta_{1c} &= -C_{M,x} / \frac{\partial C_{M,y}}{\partial \theta_{1c}}
\end{aligned} \tag{5}$$

Similar approaches has been used in Refs. [37–39]. Yang et al. [37] used a lifting-line technique external to the flow solver to obtain the derivatives of the rotor performance parameters. An alternative expensive approach is presented in Refs. [38, 39], where the flow solver is used to determine the derivatives of the rotor performance parameters by repeating the simulation with slightly different values of the angles  $\theta_0$ ,  $\theta_{1c}$  and  $\theta_{1s}$  in succession. An accurate estimate of the derivatives requires a converged flow solution for each of these different control settings. Typical trimmed rotor simulations involved upto 35 revolutions of the rotor in total.

## 2.4 CSD Solver and Aeroelastic Coupling

A modal approach was chosen in order to compute the deformed shape of the blade. The final deformation is then considered as a combination of the eigenvectors of the blade. The modes shape and frequencies are first computed using the NASTRAN [40] CSD code. The blade structure is represented as a set of beam elements located on the elastic axis of the blade. The non-linear *PBEAM* elements of NASTRAN [40] were used. For each section, a rigid bar (*RBAR* element) without any structural properties and rigidly linked to the chord nodes was added in front of the trailing edge and aft of the leading edge in order to assess the displacement of the blade surface. The blade lead-lag stiffness is represented as a linear elastic element. An example of such model is shown in forward flight computations presented in section VII.

The mode shapes and frequencies are obtained through NASTRAN by performing a non-linear static calculation (SOL106). The data requested by NASTRAN for a *PBEAM* beam element are the flapping and chordwise area moments of inertia and the linear mass. Other properties can be added introducing the offset between the beam element axis and the blade elastic axis as well as the radius of gyration, that allows coupling between the flapwise, chordwise and torsional deformations. These data have to be specified at least at the root of the element, but can also be specified at other locations of the element.

The structural model of a blade usually contains less elements than the blade surface on the fluid mesh. Therefore, the structural solution has to be interpolated on the blade surface. The deformation of the fluid mesh is done in three main steps. Firstly, the constant volume tetrahedron (CVT) method [41] is used to interpolate the deformed shape of the blade surface. Secondly, the block vertices are moved accordingly to the spring analogy method. Finally, the full mesh is regenerated with a trans-finite interpolation (TFI) [42]. The interpolation process is described in details in [24–26].

For forward flying rotors, the modal approach is used to lower the cost of computing the blade deformations. It expresses the blade deformation as a function of the blade eigenmodes. The blade shape  $\phi$  is then described as a sum of eigenvectors  $\phi_i$  representing the blade displacements for each eigenmodes multiplied by the coefficient  $\alpha_i$ :

$$\phi = \phi_0 + \sum_{i=1}^{n_m} \alpha_i \phi_i \tag{6}$$

where  $\phi_0$  is the undeformed eigenvector. The problems is then reduced to solving for the coefficients  $\alpha_i$ .

In the modal approach, the coefficients can be obtained by solving the following differential equation:

$$\frac{\partial^2 \alpha_i}{\partial t^2} + 2\zeta_i \omega_i \frac{\partial \alpha_i}{\partial t} + \omega_i^2 \alpha_i = \mathbf{f} \cdot \phi_i \tag{7}$$

where  $\mathbf{f}$  are the external forces applied to the blade projected at each structural node, and  $\zeta_i$  the structural damping coefficient.

## 3 W3-SOKOL

### 3.1 MRB Geometry

The W3-Sokol main rotor consists of four blades made out of fibre-glass. It is a soft blade in torsion that encourages the idea of the implementation of a Gurney flap in order to alter the twist distribution along the radius of the blade. Fig. 1 presents the geometry of the original MRB. The radius of the blade is along the x-axis and the leading-edge points towards the positive y-axis as the blade is rotating counter-clockwise. Although different sections of 5-digit NACA series are used along the radius, the basic section is the NACA23012M which is created by taking some camber out of the baseline NACA23012. At  $0.678R$  of the blade there is a trim tab of  $0.1c$  length and  $0.07R$  span, while from  $0.75R$  and up to the blade tip there is a trailing edge tab of  $0.05c$ . The tip of the blade is rounded as shown in Fig. 1-III. The MRB has a blunt trailing edge. All these geometrical

characteristics increased the complexity of the generated mesh. Adding a fixed Gurney within the multiblock mesh topology increased the number of nodes and required additional computational time to calculate even the hover cases. For this reason the implementation of an infinitely thin Gurney flap was essential. For forward flight, a Gurney flap of  $0.02c$  height was placed at  $0.40R$ , and had a span of  $0.25R$ , as shown in Fig. 1-I. The Gurney flap was flagged using the local mesh around the blade. This allows a normal to the trailing edge flap of infinite thickness to be simulated. The process of localising the flap and flagging cells as solid is described by Woodgade and Barakos [34]. The mesh used for the forward flight calculations consists of 27 million nodes. It is a combined C-type topology in the chordwise plane with 402 nodes along the blade and O-type topology in the spanwise plane with 196 nodes around every section of the blade. In the normal direction of the blade 64 nodes have been used. The domain is split in the rotor mesh which includes the rotor blade geometry and the hub, and the background mesh. The flow in the interface of those two meshes is interpolated using sliding planes. The whole domain is split in 5480 blocks and it is presented in Fig. 2.

### 3.2 Hover Flight

Earlier work [23] demonstrated the potential effect of a Gurney flap on the performance of the W3-Sokol rotor blade in hover. A rigid blade was first considered and the calculations were conducted at several thrust settings. The Gurney flap was extended from  $46\%R$  to  $66\%R$  and it was located at the trailing edge of the main rotor blade. Four different sizes of Gurney flaps were studied, 2%, 1%, 0.5% and 0.3% of the chord, and the biggest flap proved to be the most effective. A second study [23] considered elastic blades with and without the Gurney flap. The results were trimmed at the same thrust values as the rigid blade and indicate an increase of aerodynamic performance when the Gurney flap is used, especially for high thrust cases. Comparative performance calculations have been conducted at six different thrust targets for the rigid clean blade using the  $k - \omega$  SST turbulence model. The maximum FM of the blade did not improve, but at high thrust settings it was enhanced by 6% over the performance of the clean blade. The effect of the Gurney flap to pitch the nose of the section down was evaluated with aeroelastic calculations and it was found that the extra lift of the Gurney in combination with the extra blade twist resulted in an increased FM, which corresponds to additional weight of 120 kgs as presented in Fig. 3.

### 3.3 Forward Flight

For the aeroelastic forward flight computations, the mode shapes of the W3-Sokol MRB based on the structural model of Fig. 4 were given to the solver as an initial shape of the elastic blade. Modes up to the first torsional mode were used. These mode shapes are presented in Table 1, and they are mixed flapping, inplane, and torsional deformations, which made hard to characterise them. Fig. 5 presents the shape of the rigid and the elastic blade shapes at the back of the disk. The tip of the elastic blade is pitching down by 10 degrees compared to the rigid, while the blade is flapping more by almost 2 degrees, while the lagging angle is almost 3 degrees. The elastic rotor was trimmed at  $C_T = 0.0117$  for both clean and Gurney cases in order to evaluate the effect of the flap, while the disk pitching and rolling moments were driven to zero. Fig. 6 presents the trimming history of the computations. For the case where the Gurney was actuated the torque requirement of rotor was decreased by 3.3% which corresponds to  $40KW$ . This reduction is occurred at the retreating side of the disk because of the stall decrease. Fig. 7 presents the streamlines on separation region of the blade at  $\Psi = 270^\circ$  along with the effect of the Gurney flap. The blade shown in Fig. 7b is pitched down and the flow is less separated compared to the clean case. In fact, the observed benefits are due to the aerodynamic enhancement of the blade which allows the rotor to operate in lower collective, as well as, the aeroelastic re-shaping of the blade due to the pitching moments induced by the flap.

#### 3.3.1 Gurney flap effect along the flight envelope

Since more data was available from flights for the W3 Sokol, CFD calculations were performed in lower advance ratio and thrust requirements. The reason was to identify the effect of the Gurney flap along the full flight envelope of the W3 Sokol helicopter for the same actuation schedule of the flap. Fig. 12 presents the trimming history of the elastic rotor with and without the Gurney flap for  $\mu = 0.11$  and  $W = 6000Kg$ , as well as, a comparison against the high speed and high weight forward flight cases. It has to be noted that for a complete aeroelastic trimmed computation it takes about 250000 CPU-hours to finish. The most useful outcome of this study is the power reduction gain of the rotor because of the active Gurney flap. Fig. 13 shows the effect of the flap from hover to high speed forward flight. For this weight of the W3-Sokol the Gurney shows some benefit in hover, although it becomes very beneficial in higher thrust requirement as presented in the hover section. During forward flight the flap becomes beneficial close to  $\mu = 0.11$ . At high speed and high weight cases, the potential effect of the Gurney on the retreating blade stall alleviation enhances the aerodynamic performance of the rotor and reduces the power requirements significantly. However, Fig. 13 clearly shows that a Gurney should be deployed during hover only for high thrust requirements, while it should remain retracted at low forward flight speed.

## 4 GURNEY EFFECT ON STRUCTURAL PROPERTIES OF THE BLADE

The effect of different tip designs on the aeroelastic properties of a blade was studied using the S-76 blade. The idea is to compare that effect with the one due to adding a Gurney flap on the W3-Sokol blade. Four different tip designs are used, a

rectangular, a tapered, a swept, and a tapered-swept as presented in Fig. 8. What changes between the four designs is the mass distribution, the torsional inertia of the tip segment, and the location of the elastic axis and centre of gravity at the tip. The comparison of the modes up to  $125Hz$  between the baseline case and the tapered-swept tip design is presented in Figs. 10. It is to be noted that the different designs did not alter the characterisation of the modes and the frequencies were shifted by less than 1% compared to the baseline tip design. This outcome shows that even such differences in the design, which lead to significant changes on the aerodynamic behaviour of the blade, will not affect a lot the aeroelastic response of the blade. Fig. 9 presents the properties used in NASTRAN for three different blades, the S-76, the W3-Sokol, and the UH60A blade to get an insight of the different parameters used in the models. Finally, the effect of the additional mass of the Gurney flap actuation mechanism on the aeroelastic response of the blade was tested by distributing an additional 10% of the total mass of the blade at the sections where the Gurney flap was located. Fig. 11 presents the spoke diagram of the clean blade and a comparison against the fully instrumented blade is given in Table 2. Again, for the added mass, the mode shape characterisation was not altered by the Gurney flap mechanism, while the frequencies of the given modes were decreased up to 1.6%. As a result it seems that the uncertainty due to the Gurney flap is of the same order of magnitude with the one introduced due to the different tip shape designs.

## 5 CLOSED LOOP CONTROL

For the forward flight of the W3-Sokol rotor, CFD computations for the clean rotor were used to derive the flap actuation schedule. However, in actual helicopter flight, there must be a controller, that will actuate the Gurney flap based on some observations of flight parameters. The idea is to detect the pressure divergence at the leading edge of the blade section that is indicative of stall, and if that exceeds a threshold then the flap will be actuated. Moreover, the 1/Rev actuation of the Gurney that was used in the previous chapter could introduce limitations on the handling and trimming of the helicopter. This topic was addressed by building a generic rotorcraft and performing several linear/non-linear analysis to study its response to different control inputs.

### 5.1 2D closed loop control

A NACA23012M aerofoil section was set to pitching-translating (dMdt) motion [43]. The aim was to investigate retreating blade stall to identify  $c_P$  peaks at the suction side of a blade section that could be used for the closed loop actuation of the Gurney. During the pitching-translation computations the pressure coefficient at the leading edge increased gradually at first and then the gradient became steeper before it reduced markedly and it even reduced when the aerofoil stalled. The  $c_P$  threshold when the flow was about to separate was estimated close to 3.5. Fig. 14 compares the maximum pressure coefficient that was observed at the clean aerofoil and at the aerofoil with the active Gurney during the dMdt computations. For that particular actuation two revolutions are needed for the flow to converge before the  $c_P$  is extracted to compute the Gurney schedule. Then, the aerofoil must be trimmed at the clean mean  $C_L$  and extract the new pressure coefficient to adjust the Gurney flap deployment. After a total number of 8 revolutions, the lift is trimmed and the aerodynamic loads are presented in Figs. 15-17. Fig. 18 presents the pitching motion change of the aerofoil during the Gurney actuation and the trimming of the aerofoil. Figs. 19, 20 show the streamlines near the trailing edge for different azimuth steps and how the separated flow is reattached after the actuation of the Gurney. It should also be mentioned that the  $c_P$  limit that defines the onset of the stall is only valid when the flow is fully attached. That means that when the flow is separated and it reattaches again, then this pressure threshold is significantly higher. In that case  $c_P = 5$  is the indicative value for the Gurney retraction, as the flow seems to be completely reattached on the aerofoil after the actuation of the flap. This can be seen in Fig. 21 where the flow is visualised at different steps.

### 5.2 W3-Sokol closed loop control

Next, the pressure divergence criterion was used for the elastic W3-Sokol rotor at high advance ratio forward flight. The idea was to measure the pressure coefficient at different sections along the blade around the azimuth and identify  $\Psi$ , where part of the blade was experiencing stall. Figs. 22, 23 present the pressure coefficient at two different sections along the blade span. Based on that criterion, the new actuation schedule of the Gurney was defined as presented in Fig. 24. It is observed that it is very similar to the one used in previous chapter for the open loop control, but this time the onset and end of the actuation took place earlier. The pressure distribution was also extracted after the actuation of the Gurney and at the end of the trimming process. Before trimming the rotor at the clean case thrust setting the implementation of the Gurney leads the blade section in a deeper stall, while once the rotor was trimmed the blade was pitched down, and part of the initial stall was removed. As can be seen in Fig. 25, the maximum pressure coefficient has decreased significantly. This fact led to a further reduction of the torque requirement predicted during the open loop control for the same flight case, which is about 0.5%.

## 6 EFFECT OF GURNEY FLAP ON FULL HELICOPTER MODEL

This section describes the development of a simulation model for a Generic Light Utility Helicopter (GLUH) [44]. The model is built in FLIGHTLAB environment for handling qualities and flight control investigations. The GLUH has a conventional configuration with high-mounted tail-boom carrying fixed horizontal stabiliser and twin fins. The main rotor hub is a hingeless design with a torsion bar.

A blade element rotor module was used as the rotor model. The blade element rotor model considers rotor dynamic degrees of freedom for each individual blade, either rigid or elastic. For that study a rigid blade was assumed. It computes the airloads with respect to the local angle of attack and Mach number and calculates blade dynamic response for nonuniform blade inertial and aerodynamic properties (e.g., chord and twist).

The blade element articulated rotor model includes blade hinges for feathering, flapping, and lead-lag. The feathering hinge is modelled via control hinge, thus has no degree-of-freedom, while the flap and lead-lag hinges are modelled with dynamic hinge of one rotational degree of freedom. Flap or lead-lag stop is modelled via nonlinear torsional spring/damping with further option of spring/damping dependence. The blade stop model table data are defined based on the blade flap or blade lag angle.

For the baseline model, a Quasi-Steady aerodynamic component was used for the airload calculation on the blade elements. The blade aerodynamic segments are defined based on the equal annuli area approach. This means that the segment length becomes finer towards the tip of the blade, while the aerodynamic loads are calculated by treating the blade sections as two-dimensional panels as described before.

The NACA23012M sections was used, and the data were represented in table look-up form with lift, drag, and pitching moment coefficients tabulated against angle of attack (-180 to 180 deg) and Mach number (0-0.9 Mach). The GLUH model described in this work makes use of the Peters-He three state dynamic wake model. This model captures the uniform and first harmonic distribution of the inflow and the transient response of these inflow components in manoeuvring flight. This methodology also models the dynamic response of the inflow to manoeuvring flight and predicts the off-rotor components of inflow for use in interference modelling at the fuselage and tail.

FLIGHTLAB's Bailey rotor component is used to model the tail rotor. In the Bailey model, closed form expressions for rotor thrust and torque are obtained analytically by integrating the airloads over the rotor blade span and averaging them over the azimuth. Only rotor coning is considered and hence there is no provision for blade cyclic pitch inputs. The induced velocity is computed from a uniform inflow model and included in the model. The following assumptions are employed in the derivation of the tail rotor equations:

- 1) constant chord and linear twist,
- 2) linear lift with lift curve slope,
- 3) incompressible flow,
- 4) no individual blade dynamics, except for the steady state coning, and
- 5) uniform induced flow over the rotor.

There are several modelling options available within FLIGHTLAB for the fuselage aerodynamics, including a panel method and a simple table look-up. For the Generic model, the table look-up option was chosen where the fuselage coefficients are supplied by means of look-up tables as functions of angle of attack and sideslip angle [44].

The GLUH model uses a NACA23015 aerofoil for the horizontal stabiliser, and a NACA0012 for the vertical fins. Again the aerodynamic loads were imported by the use of 2D look-up tables based on the performance of these aerofoils.

Regarding the powerplant, two gas turbine engines PW207K of PRATT & WITNEY company with takeoff power of 630 hp each were used. The engine was modelled using the ideal engine.

Modelling the aerodynamic interactions is a challenging aspect of rotorcraft simulation. A simple and effective way of interactional modelling is by incorporating look-up tables representing the downwash/up-wash velocities at the respective aerodynamic surfaces, defined by the values of loads on the generating surface. In the absence of empirical/experimental data, the off-rotor induced velocity predicted by FLIGHTLAB's inflow model is used for the calculation of the effect of the main rotor wake on fixed aerodynamic surfaces. From the finite state dynamic wake equations the induced velocity at an arbitrary flow field point can be computed (include reference). The Generic model utilises this finite-state dynamic inference model for the main rotor wake effects. The main rotor wake interference is applied to both the empennage and the fuselage.

## 6.1 *FLIGHTLAB Validation*

Before testing the generic light utility model FLIGHTLAB was validated using the UH-60 Black Hawk helicopter. The model was built by Advanced Rotorcraft Technology [?] and the power coefficient was compared against flight test data [45] and theory predictions based on the script presented in the Appendix A, as well as numerical predictions by CAMRAD II [46]. Fig. 27 presents the power coefficient for different flight speeds. FLIGHTLAB gave good predictions between medium and high speed although it did not agree with the flight test in hover case. Moreover, the accuracy of the calculation degrades at high gross weight the same way it was observed by Yeo et al. [46] at their study.

## 6.2 *Handling Qualities*

The main purpose of building this generic model was the observation of the Gurney flap effect on the trimming and the handling qualities of a helicopter. Typically a 4 per rev actuation of plain flaps has been used on rotorcraft. However, in that study a 1 per rev actuation was implemented, which could introduce additional moments on the helicopter and result in difficulties during trimming or deterioration of the handling qualities. A comparison between nonlinear response of the body pitch rate and acceleration to a sinusoidal collective input is presented in Fig. 28 to evaluate the effect of the Kazan controller with the observers against a simple PID controller. The behaviour of the two systems was very different. The main Difference is observed

on the stability. When the PID is used the model becomes very unstable and once it starts diverging from the trim condition it never goes back to the equilibrium point. However, when the robust controller is implemented the model becomes stable again and it goes back to the equilibrium within very short time. Regarding the handling qualities of the model, FLIGHTLAB is in general able to derive them. However, only one of the available tests produced meaningful results and it is used to compare the effect of the designed controller on improving the manoeuvrability of the rotorcraft. This test was related to hover and low speed requirements and especially to small-amplitude pitch (roll) attitude response to control inputs. Based on ADS-33E-PRF [47] this criterion has requirements on bandwidth and phase delay to prevent tendency of pilot induced oscillation (PIO). The mid-term response characteristics shall apply at all frequencies below the bandwidth frequency. FLIGHTLAB generated the damping ratio of roll attitude response  $\zeta$ , and the natural frequency of roll attitude response  $\omega_n$  for the model with and without the designed controller. For the case without the controller the following results obtained:  $\zeta = 0.12$ , and  $\omega_n = 2.89 \text{ rad/s}$ , while for the case with the controller it produced  $\zeta = 0.40$ , and  $\omega_n = 0.39$ . Based on the Aeronautical Design Standard Performance Specification ADS-33E-PRF [47] the limits on pitch (roll) oscillations are presented below. According to those limits the model can not be qualified (x,y:-0.3468, 2.867, level >3), but when the controller is used the level improves to level 1. This fact clearly presents the ability of the designed controller to improve the dynamic characteristics of the rotorcraft. Moreover, when the Gurney flap is implemented in the model the result in Fig. 29 clearly shows that it does not affect the rotorcraft handling qualities.

## 7 CONCLUSIONS AND FUTURE WORK

In this work the effect of the Gurney flap on the overall flight envelope of a helicopter was studied. The Gurney flap on W3-Sokol blade in hover did not change the maximum figure of merit, but it enhanced it at medium to high thrust settings. The power requirement was also decreased in such a way that for the typical thrust case the rotor increased its loading capability by 220 kg.

In forward flight, the flap was used efficiently to alleviate the retreating blade stall. The W3-Sokol was studied again at high speed flight, and the Gurney removed most of the separated flow. As a result, the rotor torque decreased by 3.3%. The flap was tested at two flight speeds and two thrust settings as flight test data were available, and it proved to be effective above  $\mu = 0.11$  at maximum gross weight of the helicopter.

Some significant remarks regarding the stall identification and the actuation of the Gurney flap were observed. The active actuation of the flap can be implemented on real helicopters by observing the pressure on the suction side of the rotor blades. If the pressure diverges from a threshold, then the flap would be actuated. This 1/rev actuation might cause vibration issues and alter the trimming capability of the helicopter. For that reason, a generic light utility helicopter was built and tested on FLIGHTLAB with and without an active Gurney. The results showed that the flap will not change neither the trimming ability of the model nor its handling qualities if there is a robust controller on the helicopter. Another issue was the possible effect of the flap on the structural dynamics of the blade. Thus, 10% of the original mass of the blade was distributed additionally on the blade, along the location of the Gurney, and a static analysis was conducted. The mode shapes of the blade were not affected by the flap, while the frequencies of the modes at the nominal rotor speed were decreased by less than 2%. In fact, the uncertainty due to the Gurney was of the same order of magnitude of the one introduced by different tip shape designs tested for an S-76 blade.

To conclude, the potential effect of an active Gurney flap on the main rotor as well as on the response of the helicopter were studied using coupled fluid-structure dynamics. It was shown that the flap can enhance the performance of helicopters, especially at high thrust requirements, as it is an efficient flow control device for retreating blade stall alleviation. Some of the observed benefits are due to the aeroelastic re-shaping of the blade due to the pitching moments induced by the flap. However, experimental data on rotors with active Gurney flaps are essential for further validation of the code and understanding of the Gurney effect on rotor aerodynamics.

In future efforts should be directed towards the addition of the fuselage in CFD computations to study its interaction with the altered rotor wake due to the Gurney. Moreover, the effect of the flap can be further optimised by implementing multiple flaps along the rotor blade. Apart from the pressure divergence criterion, that was put forward to detect stall, other criteria should also be investigated. Finally, the active Gurney flap should be considered as a means to offload the advancing side of the rotor, and its effect should be investigated on rigid blades as well.

### *Acknowledgements*

The financial support via the IMESCON Marie Curie ITN project (grant agreement number: 264672), the release of the W3 Sokol main rotor blade geometry by PZL Swidnik, the use of the computing centre TASK of Gdansk, Poland, and the contribution of Axsym Engineering in the post-processing of the flight test data are gratefully acknowledged.

## REFERENCES

- [1] Wang, J. J., Li, Y. C., and Choi, K. S., "Gurney flap - Lift enhancement, mechanisms and applications," *Progress in Aerospace Sciences*, Vol. 44, 2008, pp. 22–47.
- [2] Liebeck, R. H., "Design of Subsonic Airfoils for High Lift," *Journal of Aircraft*, Vol. 15, No. 9, Sept 1978, pp. 547–561.
- [3] Jeffrey, D. and Zghang, X., "Aerodynamics of Gurney Flaps on a Single-Element High-Lift Wing," *Journal of Aircraft*, Vol. 37, No. 2, 2000, pp. 295–301.
- [4] Troolin, D. R., Longmire, E. K., and Lai, W. T., "Time Resolved PIV Analysis of Flow over a NACA 0015 Airfoil with Gurney Flap," *Experiments in Fluids*, Vol. 41, 2006, pp. 241–254.
- [5] Lee, T. and Su, Y. Y., "Lift Enhancement and Flow Structure of Airfoil with Joint Trailing-Edge Flap and Gurney Flap," *Experiments in Fluids*, Vol. 50, 2011, pp. 1671–1684.
- [6] Tang, D. and Dowell, E. H., "Aerodynamic Loading for an Airfoil with an Oscillating Gurney Flap," *Journal of Aircraft*, Vol. 44, No. 4, 2007, pp. 1245–1257.
- [7] Chow, R. and Van Dam, C. P., "Unsteady Computational Investigations of Deploying Load Control Microtabs," *Journal of Aircraft*, Vol. 43, No. 5, Sept–Oct 2006, pp. 1458–1469.
- [8] Baker, J. P., Standish, K. J., and Van Dam, C. P., "Two-Dimensional Wind Tunnel and Computational Investigation of a Microtab Modified Airfoil," *Journal of Aircraft*, Vol. 44, No. 2, 2007, pp. 563–572.
- [9] Kinzel, M. P., Maughmer, M. D., and Duque, E. P. N., "Numerical Investigation on the Aerodynamics of Oscillating Airfoils with Deployable Gurney Flaps," *AIAA Journal*, Vol. 48, No. 7, 2010, pp. 1457–1469.
- [10] Gai, S. L. and Palfrey, R., "Influence of Trailing-edge Flow Control on Airfoil Performance," *Journal of Aircraft*, Vol. 40, No. 2, 2003, pp. 332–337.
- [11] Yeo, H., "Assessment of Active Controls for Rotor Performance Enhancement," *Journal of the American Helicopter Society*, Vol. 53, No. 2, 2008, pp. 152–163.
- [12] Jeffrey, D., Zhang, X., and Hurst, D. W., "Aerodynamics of Gurney Flaps on a Single-element High-lift Wing," *Journal of Aircraft*, Vol. 37, No. 2, 2000, pp. 295–301.
- [13] Maughmer, M. D. and Bramesfeld, G., "Experimental Investigation of Gurney Flaps," *Journal of Aircraft*, Vol. 45, No. 6, 2008, pp. 2062–2067.
- [14] Min, B., Sankar, L. N., Rajmohan, N., and Prasad, J. V. R., "Computational investigation of Gurney flap effects on rotors in forward flight," *Journal of Aircraft*, Vol. 46, No. 6, 2009, pp. 1957–1964.
- [15] Padthe, A. K., Liu, L., and Friedmann, P. P., "Numerical Evaluation of Microflaps for on Blade Control of Noise and Vibration," *Collection of Technical Papers - AIAA/ASME/ASCE/AHS/ASC Structures, Structural Dynamics and Materials Conference, Denver, USA*, 2011.
- [16] Bae, E. S. and Gandhi, F., "Upstream Active Gurney Flap for Rotorcraft Vibration Reduction," *AHS International, 2012, Texas, USA*, Vol. 2, pp. 1354–1362.
- [17] Milgram, J., Chopra, I., and Straub, F., "Rotors with trailing edge flaps: Analysis and comparison with experimental data," *Journal of the American Helicopter Society*, Vol. 43, No. 4, 1998, pp. 319–332.
- [18] Viswamurthy, S. R. and Ganguli, R., "An optimization approach to vibration reduction in helicopter rotors with multiple active trailing edge flaps," *Aerospace Science and Technology*, Vol. 8, No. 3, 2004, pp. 185–194.
- [19] Yeo, H., "Assessment of Active Controls for Rotor Performance Enhancement," *AHS International, 2006, Phoenix, USA*, Vol. 2, pp. 935–953.
- [20] Cheng, R. P. and Celi, R., "Optimum two-per-revolution inputs for improved rotor performance," *Journal of Aircraft*, Vol. 42, No. 6, 2005, pp. 1409–1417.
- [21] Gagliardi, A. and Barakos, G. N., "Analysis and design of a flap-equipped low-twist rotor for hover," *Journal of Aircraft*, Vol. 46, No. 1, 2009, pp. 74–84.
- [22] Lorber, P., Hein, B., Wong, J., and Wake, B., "Rotor Aeromechanics Results from the Sikorsky Active Flap Demonstration Rotor," *AHS International*, Vol. 1, 2012, pp. 553–568.

- [23] Pastrikakis, V. P., Steijl, R., and Barakos, G. N., "Computational Aeroelastic Analysis of a Hovering W3 Sokol Blade with Gurney Flap," *Journal of Fluids and Structures*, , No. 1763, 2014.
- [24] Dehaeze, F. and Barakos, G. N., "Hovering rotor computations using an aeroelastic blade model," *Aeronautical Journal*, Vol. 116, No. 1180, 2012, pp. 621–649.
- [25] Dehaeze, F. and Barakos, G. N., "Mesh deformation method for rotor flows," *Journal of Aircraft*, Vol. 49, No. 1, 2012, pp. 82–92.
- [26] Dehaeze, F. and Barakos, G. N., "Aeroelastic CFD computations for rotor flows," *37th European Rotorcraft Forum, Vergiate and Gallarate, Italy*, 2011, pp. 143–162.
- [27] Steijl, R., Barakos, G., and Badcock, K., "A framework for CFD analysis of helicopter rotors in hover and forward flight," *International Journal for Numerical Methods in Fluids*, Vol. 51, No. 8, 2006, pp. 819–847.
- [28] Steijl, R. and Barakos, G., "Sliding Mesh Algorithm for CFD Analysis of Helicopter Rotor-Fuselage Aerodynamics," *International Journal for Numerical Methods in Fluids*, Vol. 58, 2008, pp. 527–549.
- [29] Barakos, G., Steijl, R., Badcock, K., and Brocklehurst, A., "Development of CFD Capability for Full Helicopter Engineering Analysis." 31st European Rotorcraft Forum, 2005, Florence, Italy, 2005.
- [30] Osher, S. and Chakravarthy, S., "Upwind schemes and boundary conditions with applications to Euler equations in general geometries," *Journal of Computational Physics*, , No. 50, 1983, pp. 447–481.
- [31] Van Albada, G. D., Van Leer, B., and Roberts, W., "A comparative study of computational methods in cosmic gas dynamics," *Astron. Astrophysics*, Vol. 108, 1982, pp. 76.
- [32] Jameson, A., "Time Dependent Calculations Using Multigrid, with Applications to Unsteady Flows Past Airfoils and Wings," *10th Computational Fluid Dynamics Conference, Honolulu, HI*, 1991, AIAA-91-1596.
- [33] Steijl, R. and Barakos, G., "A Computational Study of the Advancing Side Lift Phase Problem," *Journal of Aircraft*, Vol. 45, No. 1, 2008, pp. 246–257.
- [34] Woodgate, M. and Barakos, G. N., "Rotor Computations with Active Gurney Flaps," *38th European Rotorcraft Forum, Amsterdam, Netherlands*, , No. 54, 2012.
- [35] Woodgate, M., Pastrikakis, V., and Barakos, G. N., "Rotor Computations with Active Gurney Flaps," ERCOFTAC international symposium "Unsteady separation in fluid-structure interaction", Mykonos, Greece, 2013.
- [36] R. Steijl, G. Barakos, and K. Badcock, "A framework for CFD analysis of helicopter rotors in hover and forward flight," *International Journal for Numerical Methods in Fluids*, Vol. 51, No. 8, 2006, pp. 819–847.
- [37] Yang, Z., Sankar, M., Smith, M., and Bauchau, O., "Recent improvements to a hybrid method for rotors in forward flight," *J. Aircraft*, Vol. 39, No. 5, 2002, pp. 804–812.
- [38] Van der Ven, H. and Boelens, O., "A framework for aeroelastic simulations of trimmed rotor systems in forward flight," *European Rotorcraft Forum, Marseille*, September 14-16, 2004.
- [39] Park, Y. and Kwon, O., "Simulation of unsteady rotor flow field using unstructured adaptive sliding meshes," *J. American Helicopter Society*, Vol. 49, No. 4, 2004, pp. 391–400.
- [40] MSC Software Corporation, "MSC.Nastran 2005 Release Guide," 2005.
- [41] Goura, G., Badcock, K., Woodgate, M., and Richards, B., "Implicit Method for the Time Marching Analysis of Flutter," *Aeronautical Journal*, Vol. 105, No. 1046, 2001.
- [42] Dubuc, L., Cantariti, F., Woodgate, M., Gribben, B., Badcock, K., and Richards, B., "A Grid Deformation Technique for Unsteady Flow Computations," *International Journal for Numerical Methods in Fluids*, Vol. 32, No. 3, 2000, pp. 285–311.
- [43] Woodgate, M. A. and Barakos, G. N., "Implicit computational fluid dynamics methods for fast analysis of rotor flows," *AIAA Journal*, Vol. 50, No. 6, 2012, pp. 1217–1244.
- [44] V.I.Garkushenko, S.S.Vinogradov, and G.N.Barakos, "Robust Control Synthesis for an Unmanned Helicopter," *40th European Rotorcraft Forum, Southampton, United Kingdom, September 2014*, , No. 72.
- [45] Kufeld, R., Balough, D., Cross, J., Studebaker, K., Jennison, C., and Bousman, W., "Flight Testing of the UH-60A Airloads Aircraft," *American Helicopter Society 50th Annual Forum Proceedings, Washington, D.C., May 1994*.

[46] Yeo, H., Bousman, W. G., and Johnson, W., "Performance analysis of a utility helicopter with standard and advanced rotors," *Journal of the American Helicopter Society*, Vol. 49, No. 3, 2004, pp. 250–270.

[47] *Aeronautical Design Standard Performance Specification Handling Qualities Requirements for Military Rotorcraft*, CAGE Code 18876, 21.

[48] Garcia, A. J. and Barakos, G., "Hover Performance Predictions for the S-76 Main Rotor Blade," *AIAA 53th Aerospace Sciences Meeting and Exhibit*, Kissimmee, Florida, USA, 2015.

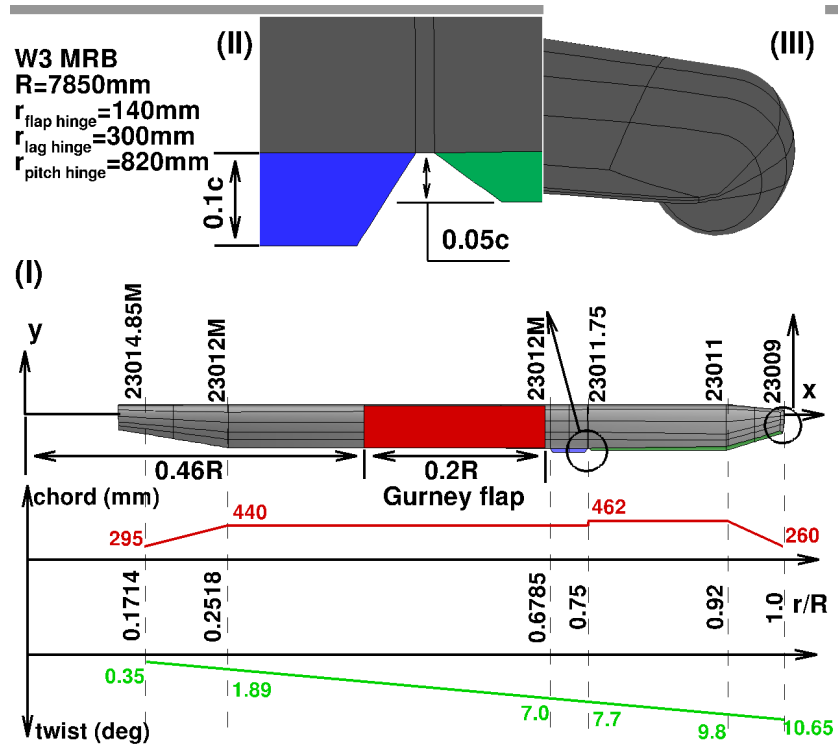


Figure 1: (I) Geometry of W3-Sokol MRB, (II) close view at the trim tab and the trailing edge tab, (III) close view at the tip.

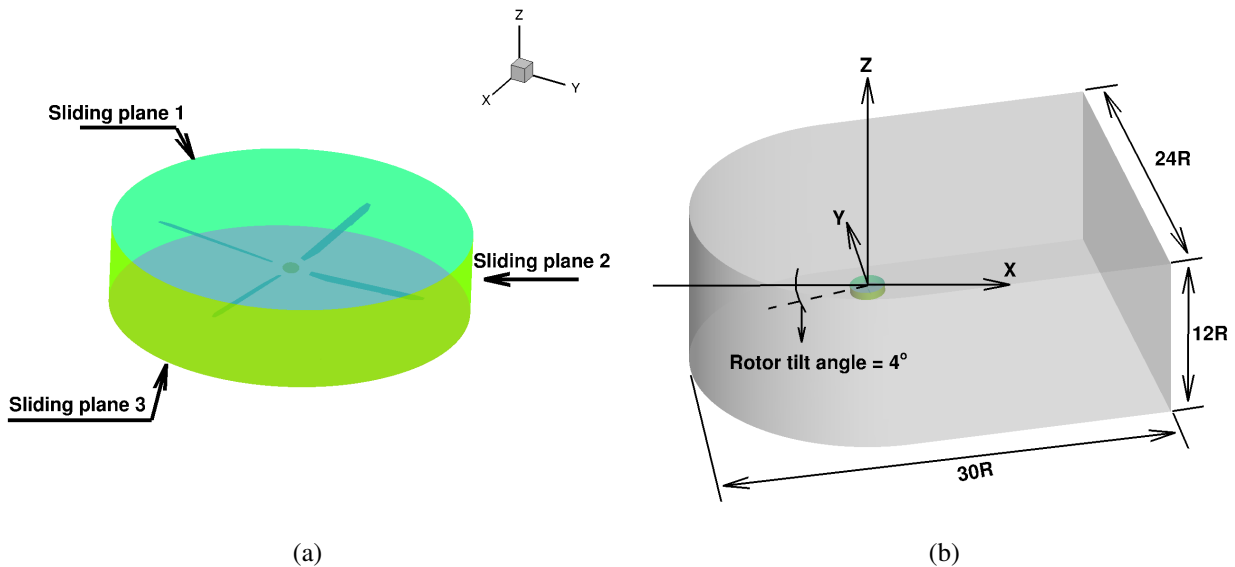


Figure 2: (a) Sliding planes around W3 MR in forward flight, and (b) overview of the computational domain used for the forward flight calculations.

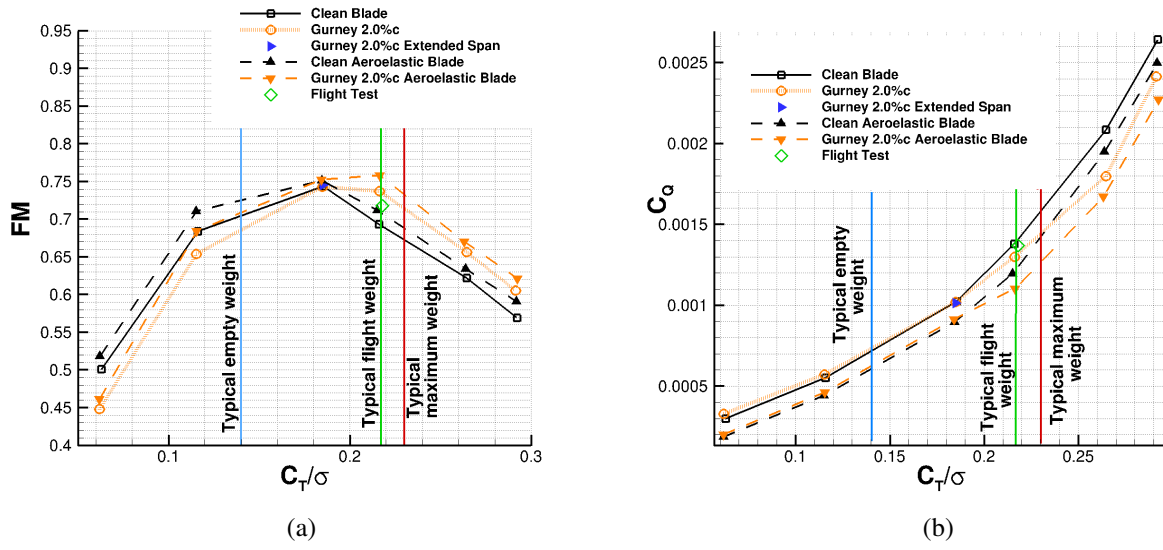


Figure 3: (a) Figure of merit, and (b) torque coefficient against normalised thrust coefficient for W3-Sokol blade in hover.

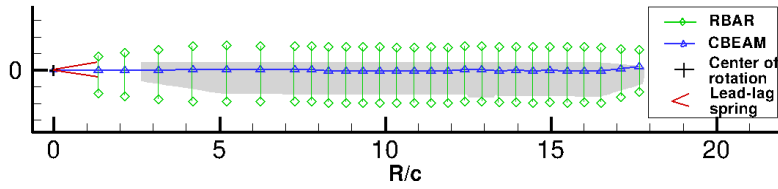


Figure 4: Structural model of W3-Sokol MRB.

| Frequency | Mode(s)   |
|-----------|-----------|
| 12.17Hz   | Flapping  |
| 21.04Hz   | Flapping  |
| 21.58Hz   | In-plane  |
| 31.42Hz   | Flapping  |
| 44.02Hz   | Flapping  |
| 57.07Hz   | In-plane  |
| 60.31Hz   | Torsional |

Table 1: Identified modes for W3 MRB rotating at 268.485rpm.

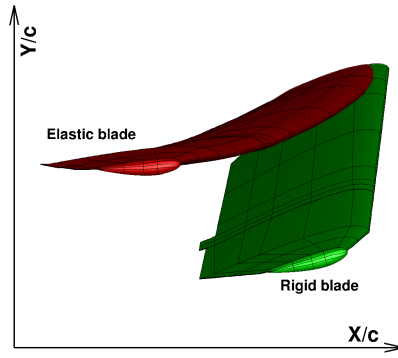


Figure 5: Visualization of the rigid and elastic W3 MRB in forward flight at  $\Psi = 0^\circ$ . Case conditions are presented in Table 2.

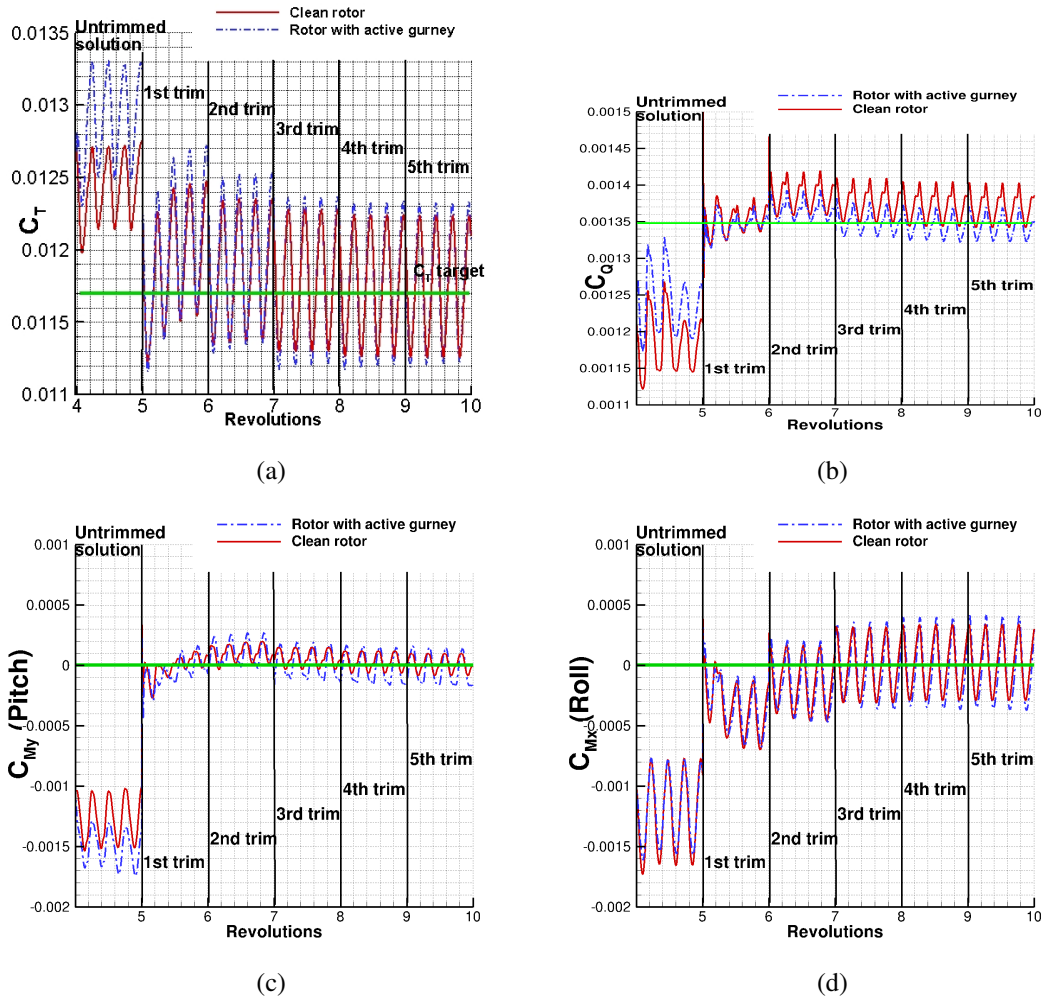
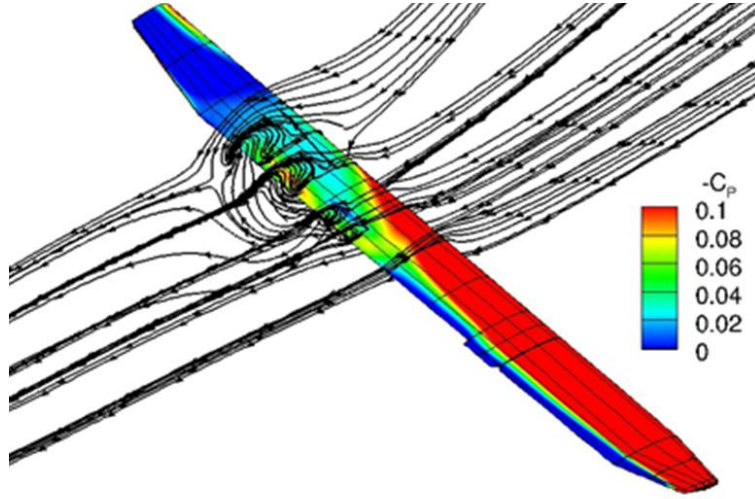
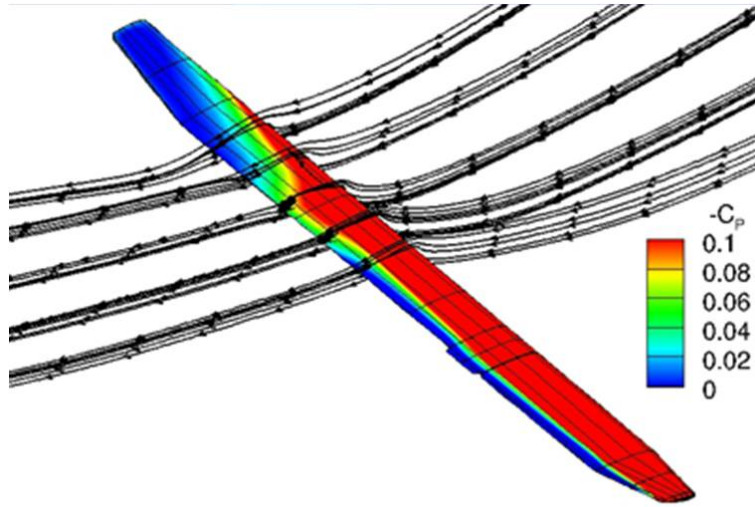


Figure 6: Trimming history of (a) thrust, (b) torque, (c) rotor disk pitching moment, and (d) rotor disk rolling moment of the elastic W3 Sokol MR in forward flight. Flight conditions are presented in Table 2.



(a) Elastic clean blade trimmed at  $C_T = 0.0117$



(b) Elastic blade with Gurney flap trimmed at  $C_T = 0.0117$

Figure 7: Visualization of the separated flow for (a) the clean blade and (b) the blade with an active gurney of  $0.02c$  at  $\Psi = 270^\circ$  of the W3 Sokol MR in forward flight. Case conditions are presented in Table 2.

| Mode Shape                | Clean blade frequency (Hz) | Blade with Gurney flap frequency (Hz) | Difference (%) |
|---------------------------|----------------------------|---------------------------------------|----------------|
| 1 <sup>st</sup> chordwise | 3.2738                     | 3.2551                                | -0.57          |
| 1 <sup>st</sup> flapping  | 4.7496                     | 4.7249                                | -0.52          |
| 2 <sup>nd</sup> flapping  | 12.3107                    | 12.1162                               | -1.58          |
| 2 <sup>nd</sup> chordwise | 19.7262                    | 19.5171                               | -1.06          |
| 3 <sup>rd</sup> flapping  | 21.763                     | 21.4257                               | -1.55          |
| 4 <sup>th</sup> flapping  | 33.479                     | 33.1141                               | -1.09          |
| 5 <sup>th</sup> flapping  | 47.973                     | 47.3254                               | -1.35          |
| 3 <sup>rd</sup> chordwise | 50.1519                    | 49.8109                               | -0.68          |
| 1 <sup>st</sup> torsional | 64.9486                    | 64.3511                               | -0.92          |
| 2 <sup>nd</sup> torsional | 84.5769                    | 83.3505                               | -1.45          |

Table 2: Mode shapes frequencies for clean blade and blade with fixed flap in hover,  $\omega = 268.48RPM$ .

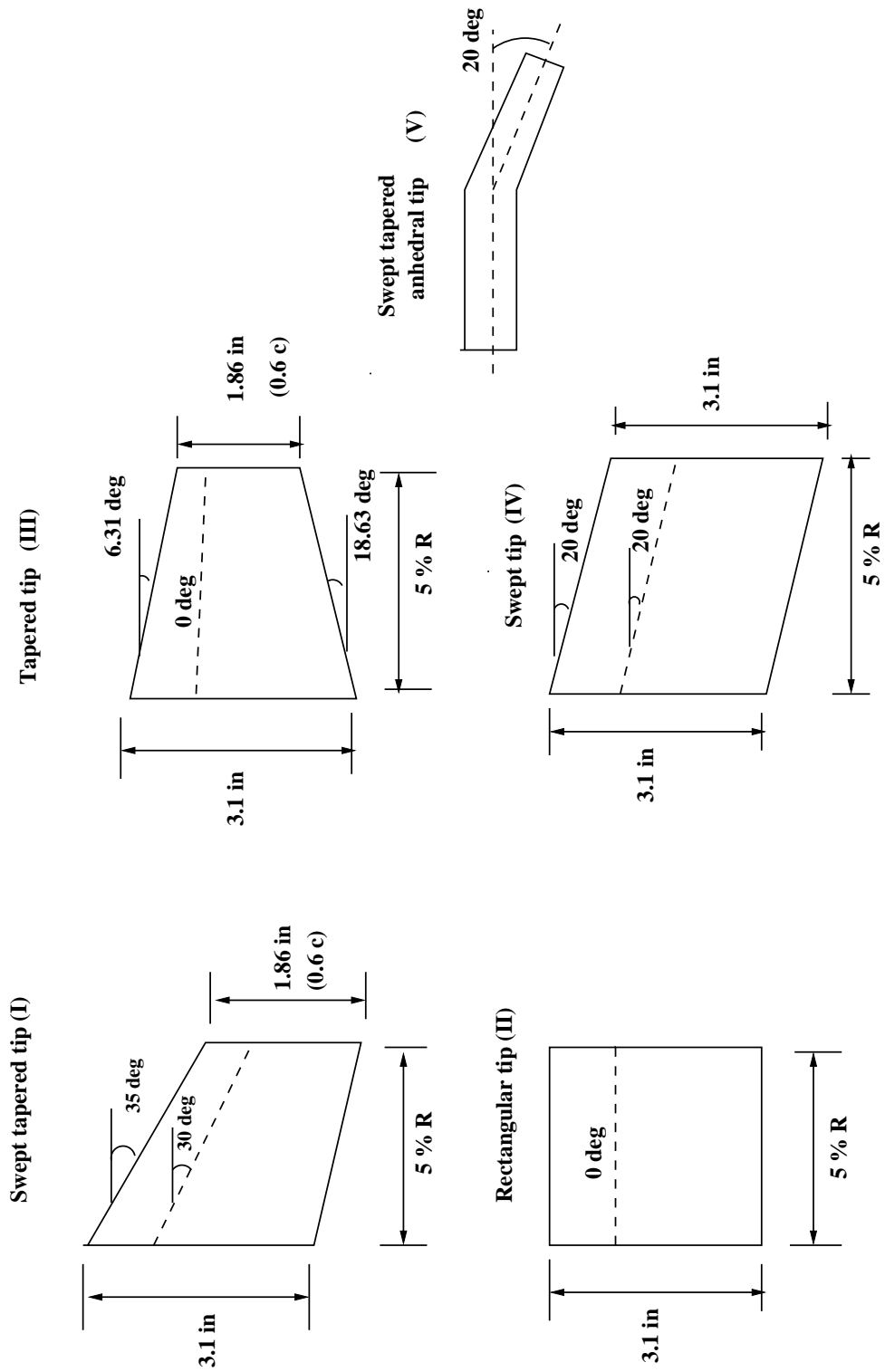


Figure 8: Different tip shapes of S-76 blade [48].

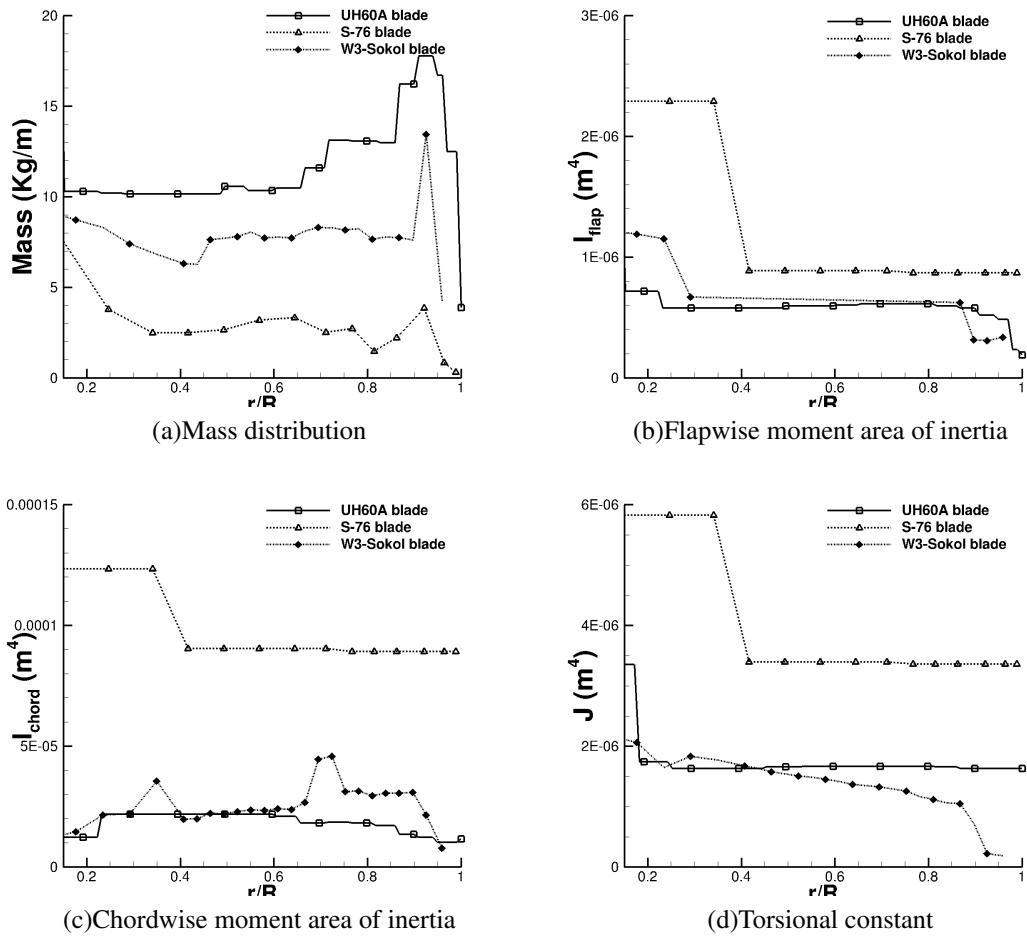


Figure 9: Structural properties of different blades used for static computations.

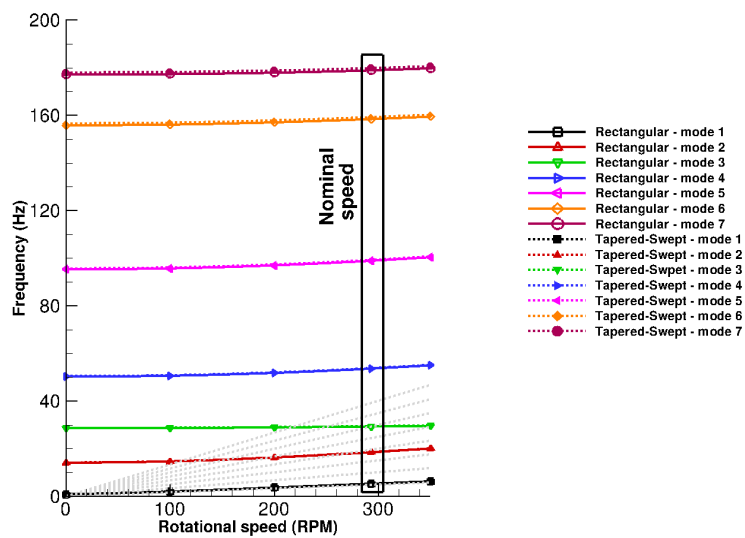


Figure 10: Spoke diagram for S-76 blade, comparison between rectangular and tapered-swept tip design.

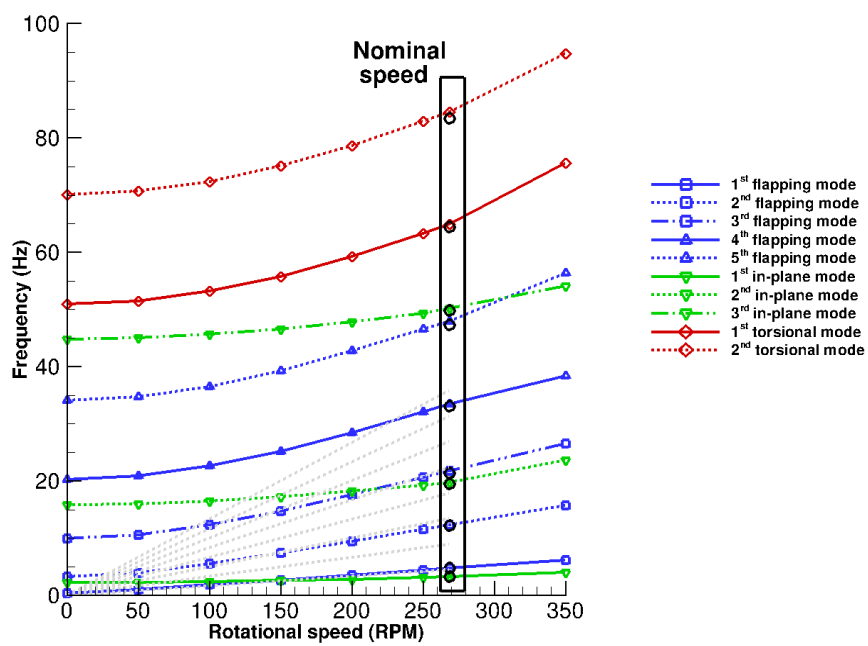
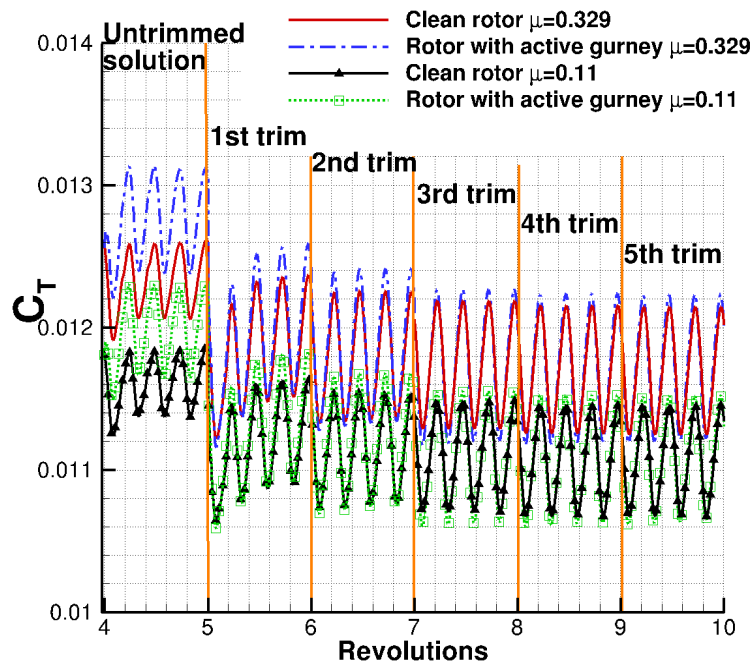
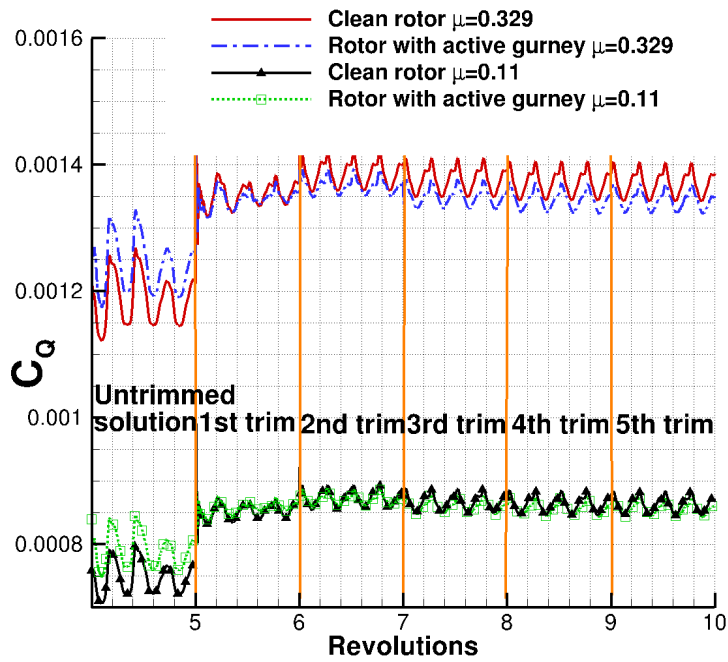


Figure 11: Spoke diagram for W3-Sokol blade. Circles are used for blade with Gurney flap.



(a)



(b)

Figure 12: Trimming history of (a) thrust, (b) torque of the elastic W3 Sokol MR in forward flight. Comparison between high speed and low speed case.

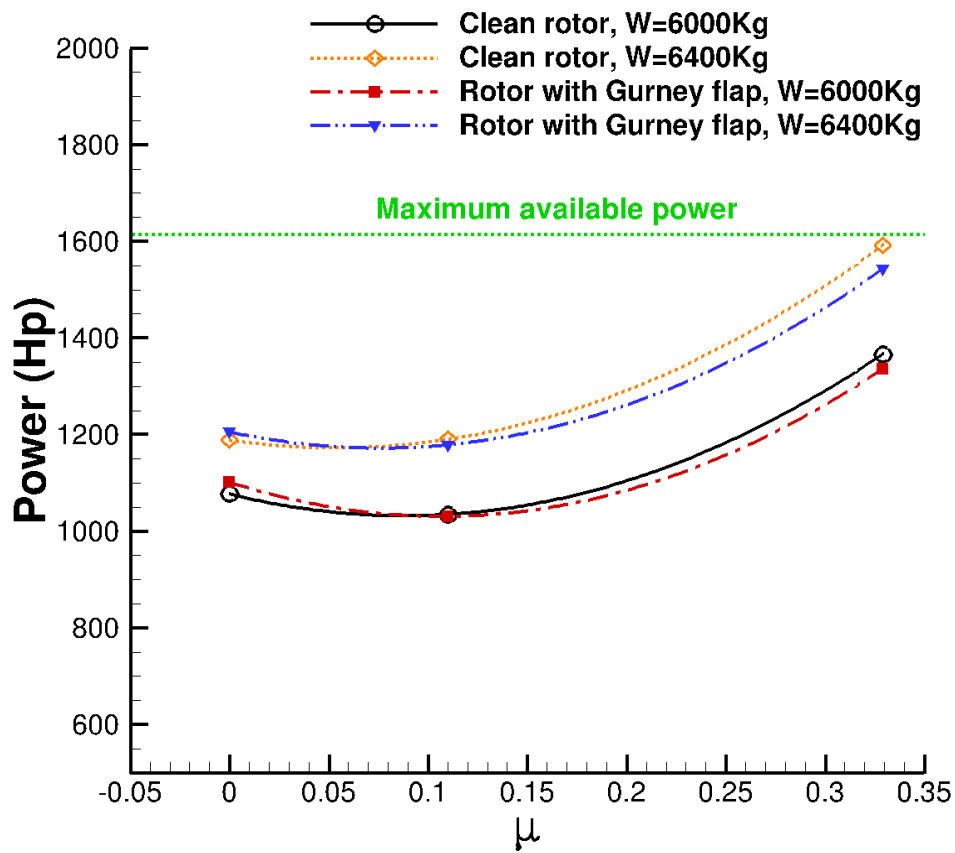


Figure 13: Power Requirements for W3 Sokol MRB along flight envelope with and without Gurney flap.

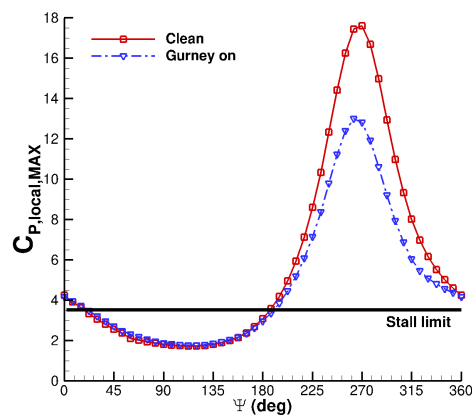


Figure 14: Pitching Translating aerofoil -  $c_{P,MAX}$  criterion.

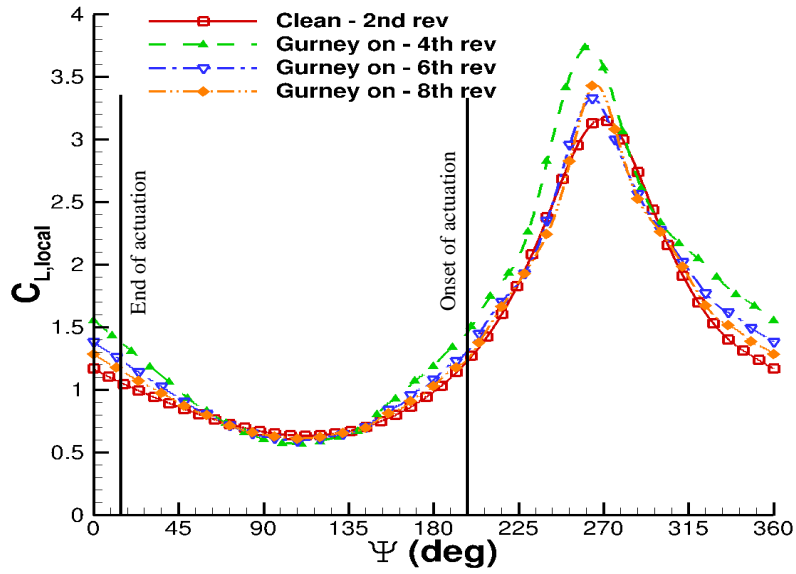


Figure 15: Pitching Translating aerofoil -  $C_L$  loads during control implementation.

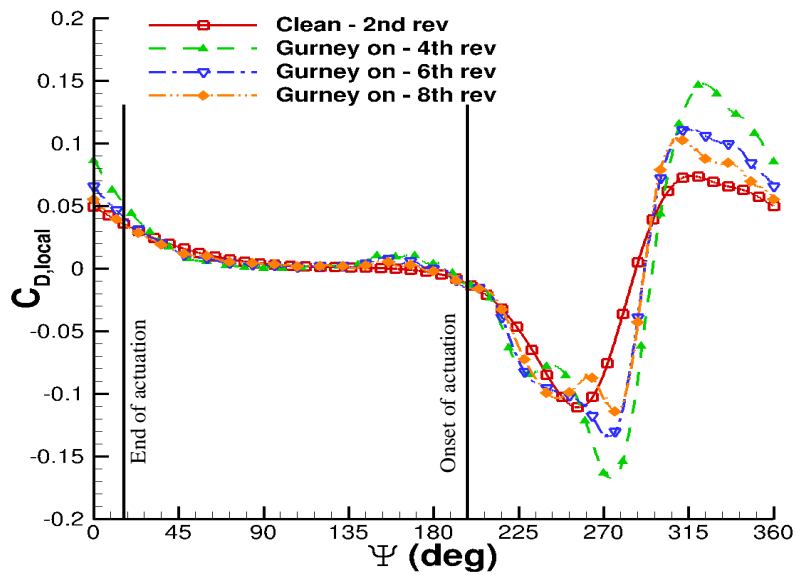


Figure 16: Pitching Translating aerofoil -  $C_D$  loads during control implementation.

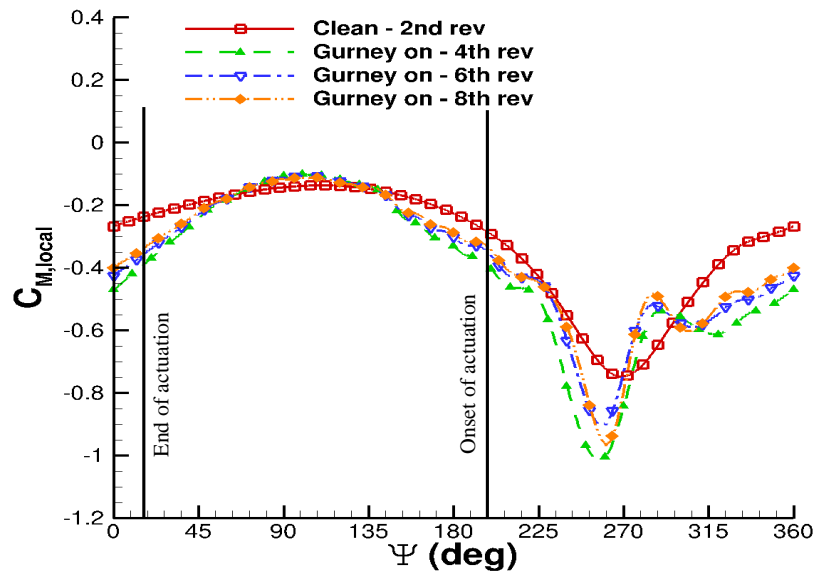


Figure 17: Pitching Translating aerofoil -  $C_M$  loads during control implementation.

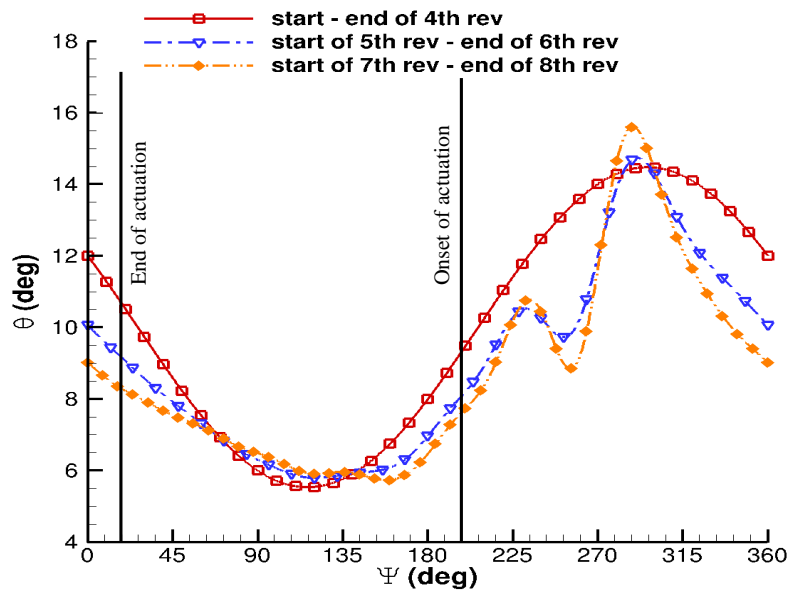


Figure 18: Pitching Translating aerofoil - pitching schedule during control implementation.

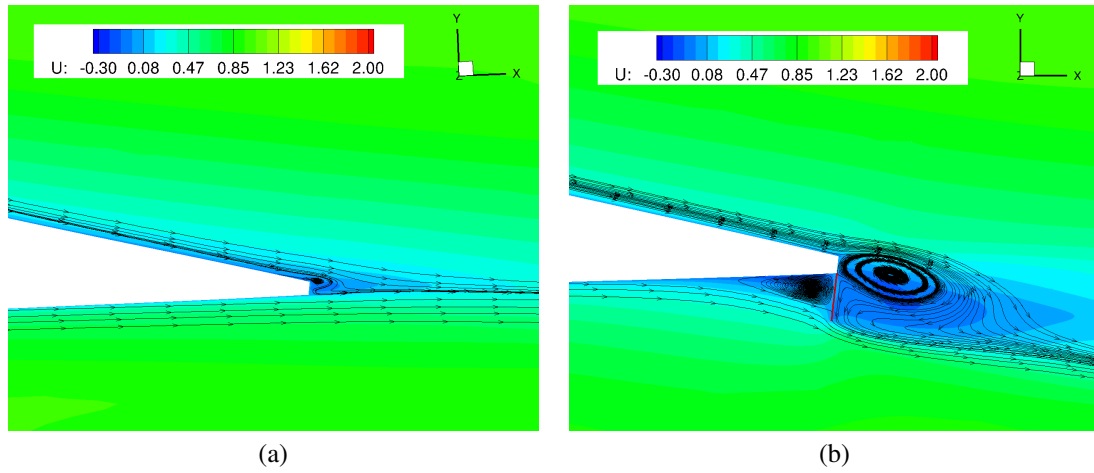


Figure 19: Pitching Translating aerofoil - streamlines near the trailing edge of the clean aerofoil (a), and of the aerofoil with active Gurney flap (b), at  $\Psi = 360deg$ .

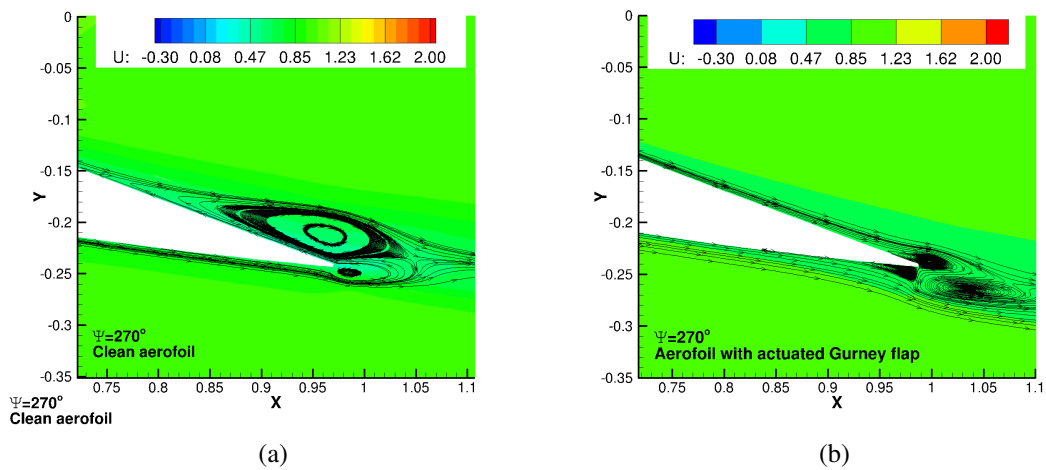
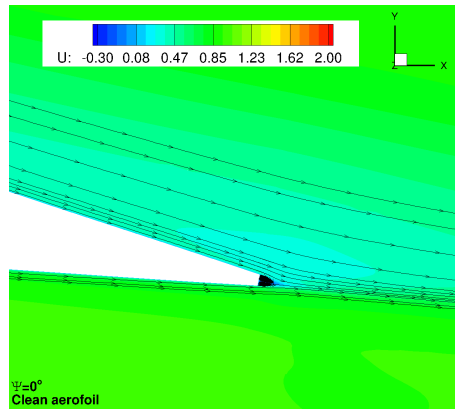
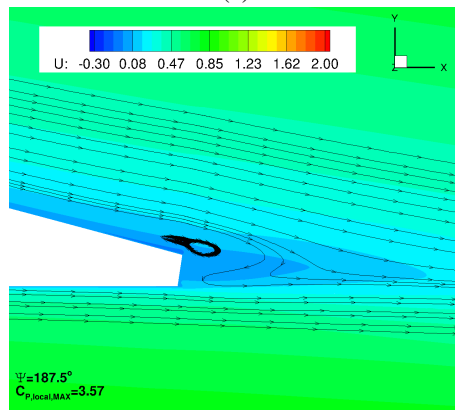


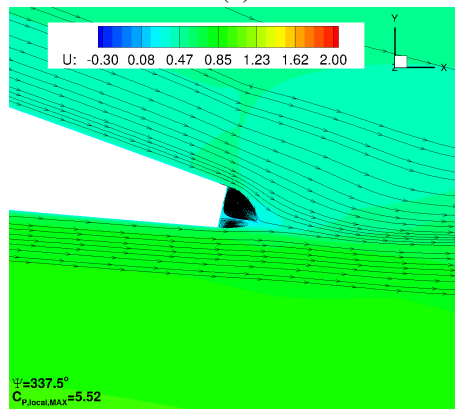
Figure 20: Pitching Translating aerofoil - streamlines near the trailing edge of the clean aerofoil (a), and of the aerofoil with active Gurney flap (b), at  $\Psi = 270deg$ .



(a)



(b)



(c)

Figure 21: Pitching Translating aerofoil - streamlines near the trailing edge of the clean aerofoil at (a)  $\Psi = 0deg$ , (b)  $\Psi = 187.5deg$ , and (c)  $\Psi = 337.5deg$ .

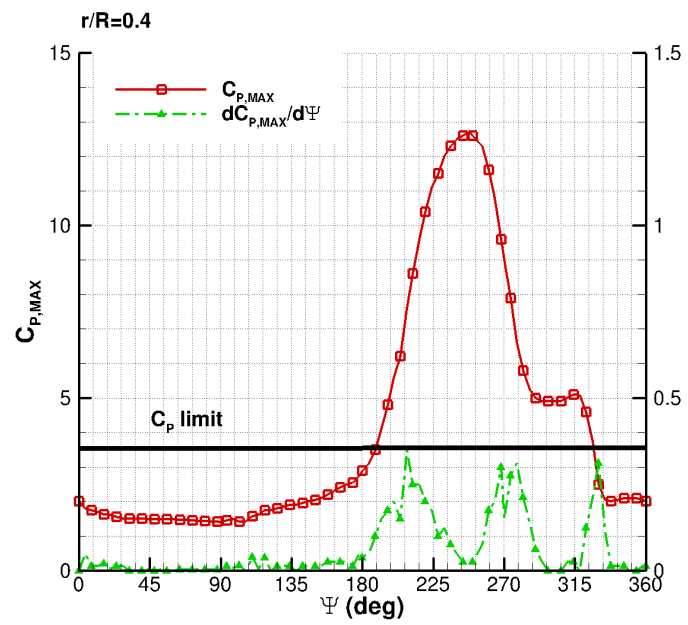


Figure 22:  $r/R = 0.4$  - Pressure divergence around azimuth.

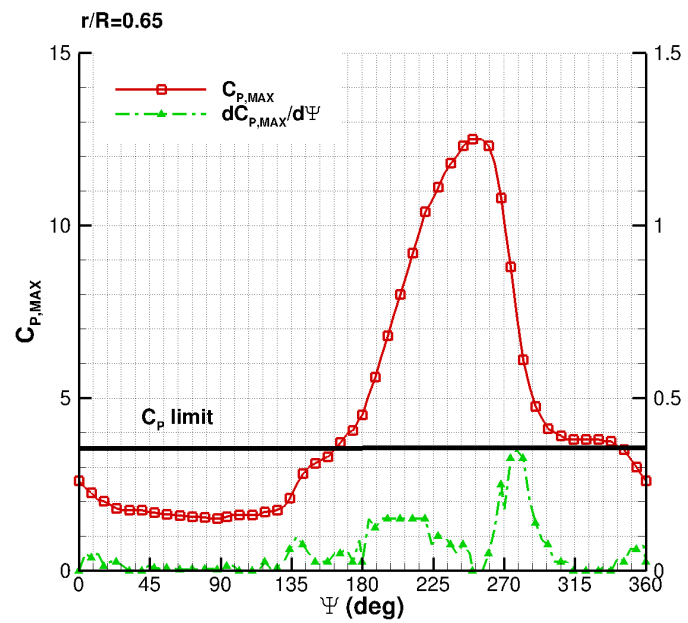


Figure 23:  $r/R = 0.65$  - Pressure divergence around azimuth.

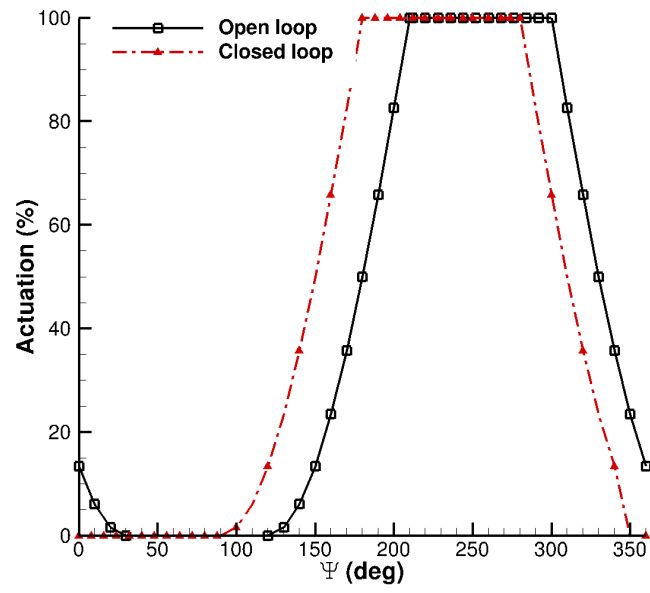


Figure 24: Gurney actuation schedule comparison against open loop.

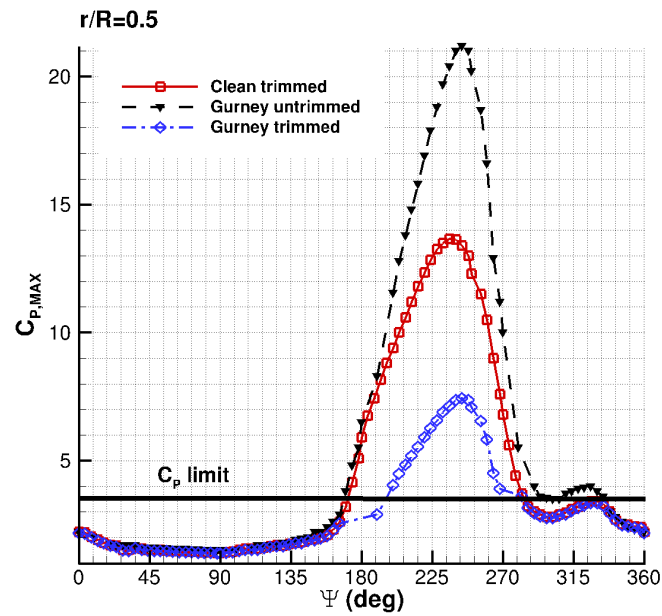


Figure 25:  $r/R=0.5$  - Pressure divergence around azimuth with Gurney flap.

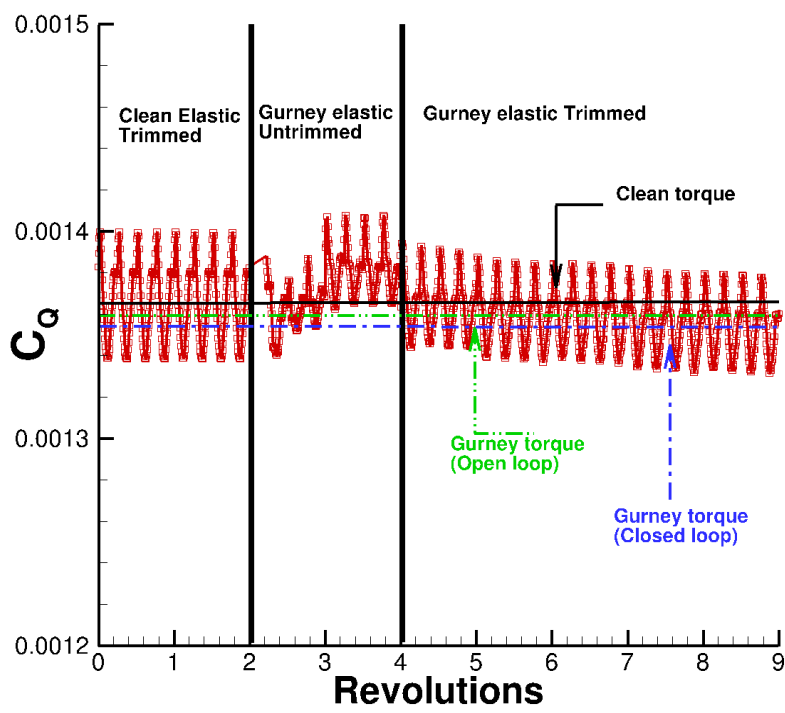


Figure 26: Torque requirement for closed loop actuation of the Gurney flap.

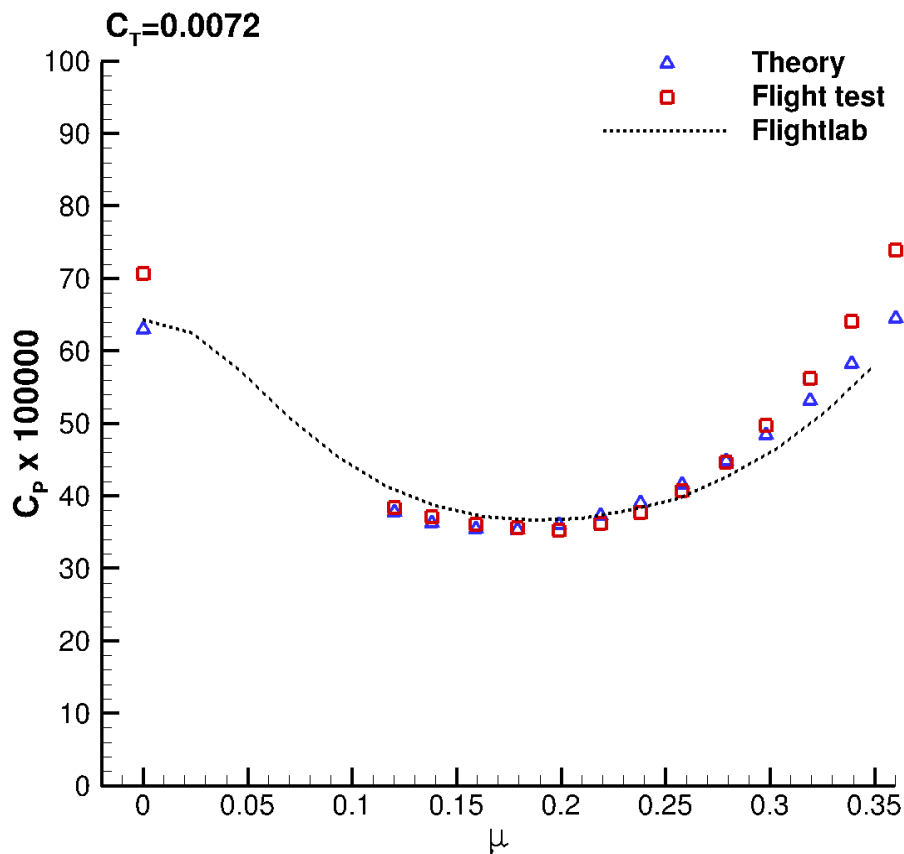


Figure 27: Power coefficient for UH-60 Black Hawk helicopter. FLIGHTLAB model against theory and flight test data [45].

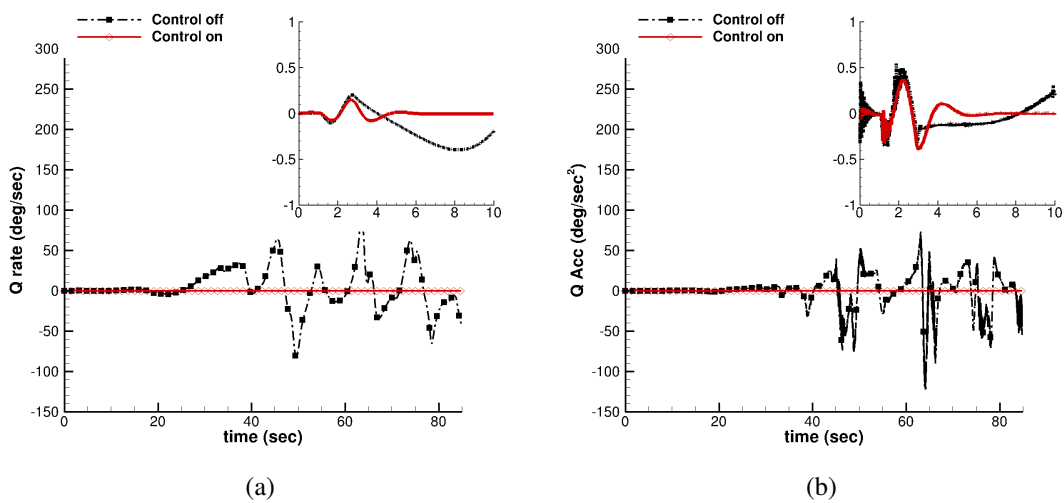


Figure 28: Nonlinear response of (a) body pitch rate and (b) body pitch acceleration to sinusoidal collective input. “Control off”, “Control on” correspond to PID and Kazan controllers respectively.

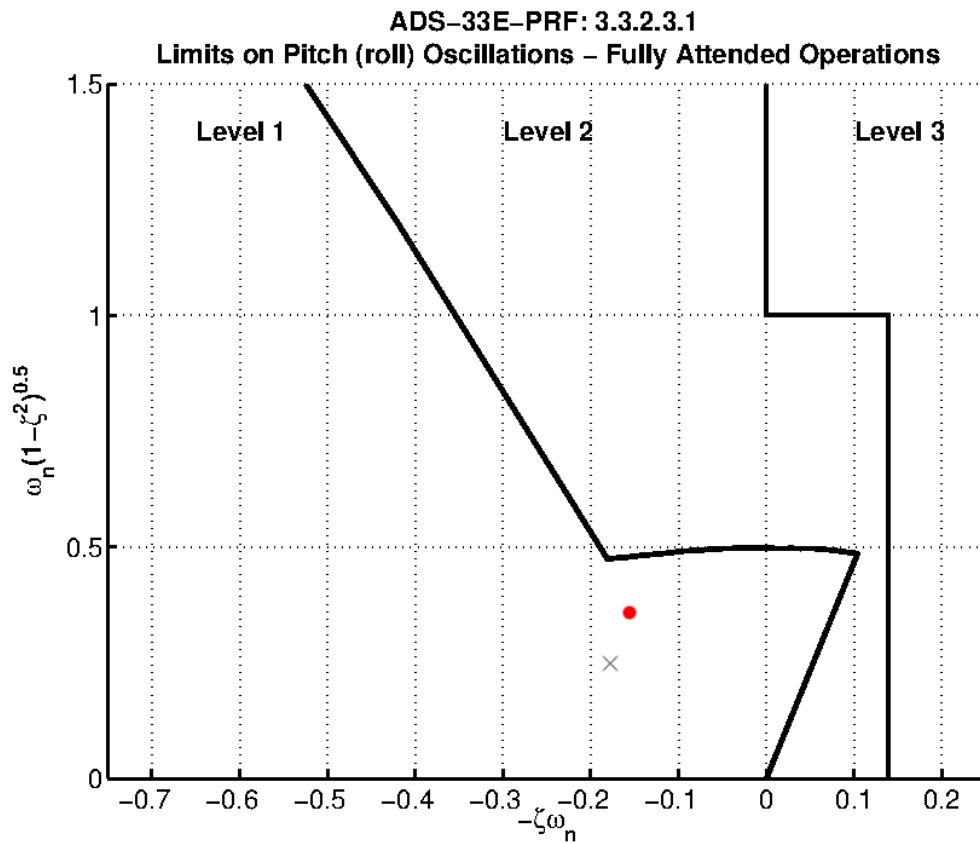


Figure 29: Limits on pitch (roll) oscillations - hover and low speed. Red dot represents the clean rotor, while cross represents the rotor with the active Gurney flap.